

A Hierarchical Max-infinitely Divisible Process for Extreme Areal Precipitation Over Watersheds

Gregory P. Bopp¹, Benjamin A. Shaby¹ and Raphaël Huser²

March 9, 2022

Abstract

Understanding the spatial extent of extreme precipitation is necessary for determining flood risk and adequately designing infrastructure (e.g., stormwater pipes) to withstand such hazards. While environmental phenomena typically exhibit weakening spatial dependence at increasingly extreme levels, limiting max-stable process models for block maxima have a rigid dependence structure that does not capture this type of behavior. We propose a flexible Bayesian model from a broader family of max-infinitely divisible processes that allows for weakening spatial dependence at increasingly extreme levels, and due to a hierarchical representation of the likelihood in terms of random effects, our inference approach scales to large datasets. The proposed model is constructed using flexible random basis functions that are estimated from the data, allowing for straightforward inspection of the predominant spatial patterns of extremes. In addition, the described process possesses max-stability as a special case, making inference on the tail dependence class possible. We apply our model to extreme precipitation in eastern North America, and show that the proposed model adequately captures the extremal behavior of the data.

Keywords max-infinitely divisible process; max-stable process; sub-asymptotic extremes; block maxima.

1 Introduction

The risk of precipitation-induced flooding (pluvial flooding) is strongly determined by the spatial extent of severe storms, and therefore, there is a need to adequately describe the spatial dependence properties of extreme precipitation. With this goal in mind, we propose a scalable model for spatial extremes that relaxes the rigid dependence structure of asymptotic max-stable models, characterizes the main modes of spatial variability using interpretable spatial factors, and allows for easy prediction at unobserved locations. The areal aspect of extreme precipitation plays a role in flood risk assessment. Precipitation falling over a single drainage basin flows into a common outlet, the aggregate effects of which can be devastating in large volumes. In 2006, heavy precipitation over the Susquehanna River basin in New York and Pennsylvania caused record high discharges along the Susquehanna River and flooding in the region, ultimately leading to federal-level disaster declarations and disaster-recovery assistance from the US Federal Emergency Management Agency (FEMA) in excess of \$227 million (Suro et al., 2009).

The last decade has seen a considerable amount of research on the spatial dependence modeling of extremes, in part because of the hazard that extreme weather events pose to human life and property. For recent reviews, see Davison et al. (2012, 2013, 2018). The classical geostatistical Gaussian process models that are ideal for modeling the bulk of a distribution have

¹Department of Statistics, Pennsylvania State University, 326 Thomas Building, University Park, PA 16802, U.S.A. Emails: gxb951@psu.edu, bshaby@psu.edu

²Computer, Electrical and Mathematical Sciences and Engineering (CEMSE) Division, King Abdullah University of Science and Technology (KAUST), Thuwal 23955-6900, Saudi Arabia. Email: raphael.huser@kaust.edu.sa

weak tail-dependence and do not enforce the specific type of positive dependence structure inherent to extremes. Two classes of models, max-stable processes (de Haan and Ferreira, 2006) and generalized Pareto processes (Ferreira and de Haan, 2014; Thibaud and Opitz, 2015), have proven to be useful tools for the modeling of spatial extremes. Max-stable process models are infinite-dimensional generalizations of the limiting models for componentwise maxima. They are asymptotically justified models for pointwise maxima over an infinite collection of independent processes after suitable renormalization, a property which has made them prime candidates for the modeling of spatial extremes. In practice, maxima are taken over large, but finite blocks (e.g., months, years). An approximation error is incurred when applying limiting models to pointwise maxima over finite blocks, and the degree of this error will depend on the rate of convergence of the modeled process as the block size grows. Furthermore, the approximation error is more pronounced when the observed process exhibits weakening spatial dependence at increasingly high quantiles. Empirical evidence has shown that environmental processes often exhibit weakening spatial dependence at more extreme levels (Huser et al., 2017a; Huser and Wadsworth, 2018; Huser et al., 2017b). Misspecifying the dependence structure can have more significant consequences when estimating aggregate quantities such as the total precipitation volume discharged by the collection of annual maxima over a region.

In this paper, we aim to extend a class of max-stable models, in order to flexibly capture spatial dependence characteristics for sub-asymptotic block maxima data, while still retaining the positive dependence structure inherent to distributions for maxima. The general class of models that we consider, which nests the class of max-stable models, are known as max-infinitely divisible (max-id) processes (Resnick, 1987, Chapter 5). Suppose a random vector \mathbf{X} has joint distribution $F_{\mathbf{X}}$, then the distribution of maxima of n independent and identically distributed (i.i.d.) replicates $\mathbf{X}_1, \dots, \mathbf{X}_n$, taken componentwise, has distribution function $F_{\mathbf{X}}^n$. The max-id property applies to the converse statement. Suppose that \mathbf{Z} is a random vector of componentwise maxima, composed from a collection of n i.i.d. vectors. Then if \mathbf{Z} has distribution function G , there exists some root distribution F such that $G(\mathbf{z}) = F^n(\mathbf{z})$, or equivalently such that $G^{1/n}(\mathbf{z}) = F(\mathbf{z})$. By continuous extension of the relation $G^{q/r} = F$ for $q, r \in \mathbb{N}$, we say that a distribution G is max-id if and only if G^s is a valid distribution for all real $s > 0$. This is always the case for univariate distributions, but may not necessarily be so for multivariate distributions. An appealing property of max-id distributions is that they allow a change of temporal support. For example, from a fitted max-id model \hat{G} to annual maxima, conclusions might directly be drawn for monthly maxima (as $\hat{G}^{1/12}$ is a valid distribution), or even daily maxima ($\hat{G}^{1/365}$ is also valid), provided temporal dependence and non-stationarity have properly been taken into account. Informally, max-id distributions are those which arise from taking componentwise maxima of i.i.d. random vectors and are therefore an appropriate class to constrain ourselves to if the goal is to model componentwise maxima. By slight abuse of language, we say that a spatial process is max-id if all its finite-dimensional distributions are max-id.

Unlike limiting max-stable and generalized Pareto process models, which have a rigid spatial dependence structure, sub-families of the broader class of max-id processes do not impose such constraints and can accommodate different spatial dependence characteristics across various levels of a distribution. It is this feature that can cause max-stable processes to fit poorly, as asymptotically independent processes may exhibit residual spatial dependence at finite levels. Extrapolation of max-stable fits to higher quantiles in this scenario can cause overestimation of the risk of concurrent extremes (Davison et al., 2013). Furthermore, the challenge of performing conditional simulation from max-stable models given observed values at many locations is a limiting factor for their use in practice (Dombry et al., 2013). The Bayesian model that we develop in the remainder of the paper permits a conditional representation that facilitates fast conditional simulation, which is useful for prediction at unobserved locations, and for handling missing values.

2 Hierarchical construction of spatial max-id models

2.1 Max-stable Reich and Shaby (2012) model

Our proposed approach is an extension of the Bayesian hierarchical model developed by [Reich and Shaby \(2012\)](#), which we review here. The [Reich and Shaby \(2012\)](#) model has found widespread interest for the modeling of spatial extremes because it possesses the max-stability property while being tractable in high-dimensions due to its conditional representation in terms of positive-stable variables (see also [Fougères et al., 2009](#) and [Stephenson, 2009](#)). Let $\alpha \in (0, 1)$ and consider a set of independent α -stable random variables $A_1, \dots, A_L \stackrel{\text{iid}}{\sim} \text{PS}(\alpha)$. Then we construct the spatial process $Z(\mathbf{s})$ as the product of two independent processes,

$$Z(\mathbf{s}) = \varepsilon(\mathbf{s})Y(\mathbf{s}), \quad (1)$$

where $\varepsilon(\mathbf{s})$ is a white noise process (i.e., an everywhere-independent multiplicative nugget effect) with $(1/\alpha)$ -Fréchet marginals, $\Pr\{\varepsilon(\mathbf{s}) \leq z\} = \exp(-z^{-1/\alpha})$, and $Y(\mathbf{s})$ is a process with residual spatial dependence, defined as an L^p -norm (for $p = 1/\alpha$) of scaled spatially varying basis functions $K_l(\mathbf{s})$, $l = 1, \dots, L$:

$$Y(\mathbf{s}) = \left\{ \sum_{l=1}^L A_l K_l(\mathbf{s})^{1/\alpha} \right\}^\alpha. \quad (2)$$

The white noise process $\varepsilon(\mathbf{s})$ functions as a nugget effect, and accounts for measurement error occurring independently of the underlying process of interest. For small α , the contribution of $Y(\mathbf{s})$ dominates that of the nugget effect, and vice-versa for large α .

[Reich and Shaby \(2012\)](#) used fixed, deterministic spatial basis functions. In other words, they assumed a Dirac prior on the space of valid basis functions, based on the following construction: let $\mathbf{v}_1, \dots, \mathbf{v}_L \in \mathcal{S} \in \mathbb{R}^p$ be a collection of spatial knots over our spatial domain of interest \mathcal{S} , and $K_l(\mathbf{s})$, $l = 1, \dots, L$, be Gaussian densities centered at each knot \mathbf{v}_l , normalized such that $\sum_{l=1}^L K_l(\mathbf{s}) = 1$ for all $\mathbf{s} \in \mathcal{S}$. The Gaussian density basis functions may be replaced with normalized functions from a much broader class while still giving a valid construction for $Y(\mathbf{s})$ in (2). A more flexible prior for the kernels $K_l(\mathbf{s})$, $l = 1, \dots, L$, is discussed in [Section 2.4](#).

[Reich and Shaby \(2012\)](#) showed that the process $\{Z(\mathbf{s}), \mathbf{s} \in \mathcal{S}\}$ has finite-dimensional distributions

$$\Pr\{Z(\mathbf{s}_1) \leq z_1, \dots, Z(\mathbf{s}_D) \leq z_D\} = \exp\left(-\sum_{l=1}^L \left[\sum_{j=1}^D \{z_j/K_l(\mathbf{s}_j)\}^{-1/\alpha} \right]^\alpha\right), \quad z_1, \dots, z_D > 0, \quad (3)$$

which follows from the fact that the Laplace transform of an α -stable variable $X \sim \text{PS}(\alpha)$ is $E\{\exp(-sX)\} = \exp(-s^\alpha)$. From (3) and the sum-to-one constraint, the marginal distributions are unit Fréchet, i.e., for all $\mathbf{s} \in \mathcal{S}$,

$$\Pr\{Z(\mathbf{s}) \leq z\} = \exp\left(-\sum_{l=1}^L \left[\{z/K_l(\mathbf{s})\}^{-1/\alpha} \right]^\alpha\right) = \exp\left\{-z^{-1} \sum_{l=1}^L K_l(\mathbf{s})\right\} = \exp(-z^{-1}), \quad z > 0.$$

Max-stability follows from (3) by checking that

$$\Pr\{Z(\mathbf{s}_1) \leq nz_1, \dots, Z(\mathbf{s}_D) \leq nz_D\}^n = \Pr\{Z(\mathbf{s}_1) \leq z_1, \dots, Z(\mathbf{s}_D) \leq z_D\}. \quad (4)$$

The max-stability property of $Z(\mathbf{s})$ makes it suitable for modeling spatial extremes in scenarios of strong, non-vanishing upper tail dependence. In [Section 2.2](#), we propose a generalized max-id model, which can better cope with weakening tail dependence.

Inference may be efficiently performed by taking advantage of the inherent hierarchical structure of the [Reich and Shaby \(2012\)](#) model, noticing that the data are independent conditional on the latent variables $\{A_l\}_{l=1}^L$, and may be written in terms of a Generalized Extreme-Value (GEV) distribution (see [Appendix A](#) for details):

$$Z(\mathbf{s})|A_1, \dots, A_L \stackrel{\text{indep}}{\sim} \text{GEV}(Y(\mathbf{s}), \alpha Y(\mathbf{s}), \alpha), \quad (5)$$

for all $\mathbf{s} \in \mathcal{S}$.

2.2 Sub-asymptotic modeling based on a max-infinitely divisible process

Despite the appealing properties of the [Reich and Shaby \(2012\)](#) model, its deterministic basis functions and its max-stability make it fairly rigid in practice. Max-id processes are natural, flexible, sub-asymptotic models, that extend the class of max-stable processes while still possessing desirable properties reflecting the specific positive dependence structure of maxima. From [\(4\)](#), we can see that max-stable processes are always max-id. Therefore, the former form a smaller subclass within the latter.

The tail dependence class strongly determines how the probability of joint exceedances of a high threshold extrapolates to extreme quantiles. A random vector $(X_1, X_2)^\top$ with marginal distributions F_1 and F_2 is said to be asymptotically independent if $\Pr\{F_1(X_1) > u \mid F_2(X_2) > u\} \rightarrow 0$ as $u \rightarrow 1$, and asymptotically dependent otherwise ([Coles et al., 1999](#)). We say that a spatial process $\{X(\mathbf{s}), \mathbf{s} \in \mathcal{S}\}$ is asymptotically independent if $X(\mathbf{s}_1)$ and $X(\mathbf{s}_2)$ are asymptotically independent for all $\mathbf{s}_1, \mathbf{s}_2 \in \mathcal{S}$, $\mathbf{s}_1 \neq \mathbf{s}_2$. Max-stable processes are always asymptotically dependent (except in the case of complete independence) and, therefore, they lack flexibility to adequately capture the tail behavior of asymptotically independent data. In this section, we propose an asymptotically independent max-id model that possesses the max-stable [Reich and Shaby \(2012\)](#) model on the boundary of its parameter space. Dependence properties are further detailed in [Section 2.6](#).

To extend the [Reich and Shaby \(2012\)](#) model to a more flexible max-id formulation, we can change the distribution of the underlying random basis coefficients $\{A_l\}_{l=1}^L$. The heavy-tailedness of the $\text{PS}(\alpha)$ distribution entails asymptotic dependence and, by construction, max-stability. To achieve asymptotic independence while staying within the class of max-id processes, we can consider a lighter tailed, exponentially tilted, positive stable distribution,

$$A_1, \dots, A_L \stackrel{\text{iid}}{\sim} \text{H}(\alpha, \delta, \theta), \quad \alpha \in (0, 1), \delta > 0, \theta \geq 0, \quad (6)$$

which was first introduced by [Hougaard \(1986\)](#), and has Laplace transform

$$\mathbb{E}\{\exp(-sX)\} = \exp\left[-\frac{\delta}{\alpha}\{(\theta + s)^\alpha - \theta^\alpha\}\right], \quad X \sim \text{H}(\alpha, \delta, \theta). \quad (7)$$

Denote the $\text{PS}(\alpha)$ density by $f_{\text{PS}}(x)$. The $\text{H}(\alpha, \delta, \theta)$ density f_{H} may be expressed in terms of f_{PS} as

$$f_{\text{H}}(x) = \frac{f_{\text{PS}}\{x(\alpha/\delta)^{1/\alpha}\}(\alpha/\delta)^{1/\alpha} \exp(-\theta x)}{\exp(\delta\theta^\alpha/\alpha)}, \quad x > 0, \quad (8)$$

for $\alpha \in (0, 1)$, $\theta \geq 0$, and $\delta > 0$ ([Hougaard, 1986](#)). An algorithm for simulating from $\text{H}(\alpha, \delta, \theta)$ is given in [Appendix C](#). When $\delta = \alpha$ and $\theta = 0$, we recover the positive stable distribution $\text{PS}(\alpha) \equiv \text{H}(\alpha, \alpha, 0)$. The parameter α controls the tail decay, with smaller values of α corresponding to heavier tailed distributions. Moreover, the density becomes increasingly concentrated around one as $\alpha \rightarrow 1$. When $\theta > 0$, the gamma distribution with shape δ and rate θ is obtained as $\alpha \rightarrow 0$.

Upon reparametrization in terms of $\alpha^* = \alpha$, $\delta^* = (\delta/\alpha)^{1/\alpha}$ and $\theta^* = (\delta/\alpha)^{1/\alpha}\theta$, we see from [\(8\)](#) that $\delta^* = (\delta/\alpha)^{1/\alpha}$ is a scale parameter, which does not affect the dependence structure of

our new model. Therefore, in the remainder of this paper, we set $\delta = \alpha$ (i.e., $\delta^* = 1$) and use $H(\alpha, \alpha, \theta)$ throughout without any loss in flexibility.

When $\delta = \alpha$ and $\theta > 0$, f_H is an exponentially tilted form of f_{PS} , where the parameter θ has the effect of exponentially tapering the tail of f_{PS} at rate θ . We will see in Section 2.6 that the exponential tilting parameter θ in the distribution of the random basis coefficients A_l is directly connected to the dependence properties of the resulting $Z(\mathbf{s})$ process.

Proposition 2.1. *Let $\{Z(\mathbf{s}), \mathbf{s} \in \mathcal{S}\}$ be defined as in (1) with $A_1, \dots, A_L \stackrel{\text{iid}}{\sim} H(\alpha, \alpha, \theta)$, $\alpha \in (0, 1)$, $\theta \geq 0$. Then, $Z(\mathbf{s})$ is max-id.*

Proof. From (7), the finite-dimensional distributions for $\{Z(\mathbf{s}), \mathbf{s} \in \mathcal{S}\}$ based on (6) are

$$\begin{aligned}
\Pr\{Z(\mathbf{s}_1) \leq z_1, \dots, Z(\mathbf{s}_D) \leq z_D\} &= \Pr\{\varepsilon(\mathbf{s}_1)Y(\mathbf{s}_1) \leq z_1, \dots, \varepsilon(\mathbf{s}_D)Y(\mathbf{s}_D) \leq z_D\} \\
&= \mathbb{E} \left(\Pr \left[\varepsilon(\mathbf{s}_1) \leq z_1 \left\{ \sum_{l=1}^L A_l K_l(\mathbf{s}_1)^{1/\alpha} \right\}^{-\alpha}, \dots, \varepsilon(\mathbf{s}_D) \leq z_D \left\{ \sum_{l=1}^L A_l K_l(\mathbf{s}_D)^{1/\alpha} \right\}^{-\alpha} \mid A_l \right] \right) \\
&= \mathbb{E} \left(\exp \left[- \sum_{j=1}^D z_j^{-1/\alpha} \sum_{l=1}^L A_l K_l(\mathbf{s}_j)^{1/\alpha} \right] \right) \\
&= \prod_{l=1}^L \mathbb{E} \left(\exp \left[-A_l \sum_{j=1}^D \{z_j / K_l(\mathbf{s}_j)\}^{-1/\alpha} \right] \right) \\
&= \exp \left(L\theta^\alpha - \sum_{l=1}^L \left[\theta + \sum_{j=1}^D \{z_j / K_l(\mathbf{s}_j)\}^{-1/\alpha} \right]^\alpha \right). \tag{9}
\end{aligned}$$

As

$$\Pr\{Z(\mathbf{s}_1) \leq z_1, \dots, Z(\mathbf{s}_D) \leq z_D\}^{1/n} = \exp \left\{ L \left(\frac{\theta}{n^{1/\alpha}} \right)^\alpha - \sum_{l=1}^L \left[\left(\frac{\theta}{n^{1/\alpha}} \right) + \sum_{j=1}^D \{nz_j / K_l(\mathbf{s}_j)\}^{-1/\alpha} \right]^\alpha \right\},$$

the finite-dimensional distributions, denoted $G(z_1, \dots, z_D; \alpha, \theta)$, from this new process satisfy $G(z_1, \dots, z_D; \alpha, \theta)^{1/n} = G(nz_1, \dots, nz_D; \alpha, \theta/n^{1/\alpha})$ for all $n \in \mathbb{N}$, and thus the process is max-id. This also confirms that the process is max-stable whenever $\theta = 0$. \square

Marginal distributions are no longer unit Fréchet when $\theta > 0$; they may be expressed as

$$G_{\mathbf{s}}(z) = \Pr\{Z(\mathbf{s}) \leq z\} = \exp \left(L\theta^\alpha - \sum_{l=1}^L \left[\theta + \{z / K_l(\mathbf{s})\}^{-1/\alpha} \right]^\alpha \right), \quad z > 0. \tag{10}$$

Bayesian and likelihood-based inference may be performed similarly as before, so this process enjoys the same computational benefits as the Reich and Shaby (2012) model, while having the traditional max-stable Reich and Shaby (2012) process as a special case on the boundary of the parameter space (i.e., when $\theta = 0$).

2.3 Spectral representation

The finite-dimensional distributions of $\{Z(\mathbf{s}), \mathbf{s} \in \mathcal{S}\}$ defined as in (1) with $A_1, \dots, A_L \stackrel{\text{iid}}{\sim} H(\alpha, \alpha, \theta)$, $\alpha \in (0, 1)$, $\theta \geq 0$, have the following spectral representation: let $\mathbf{X}_i = (X_{i,1}, \dots, X_{i,D})^\top \in [0, \infty]^D \setminus \{\mathbf{0}\}$, $i = 1, 2, \dots$, be points from a Poisson process with mean measure defined as

$$\Lambda([0, \infty]^D \setminus [0, x_1] \times \dots \times [0, x_D]) = \sum_{l=1}^L \left[\theta + \sum_{j=1}^D \{x_j / K_l(\mathbf{s}_j)\}^{-1/\alpha} \right]^\alpha - L\theta^\alpha \geq 0. \tag{11}$$

We note that the right-hand side of (11) is non-negative and monotone decreasing in each argument x_j , $j = 1, \dots, D$; therefore, Λ , endowed with the sigma-algebra of Borel sets, defines a valid Radon measure on $[0, \infty]^D \setminus \{\mathbf{0}\}$. Then, we construct the vector $\mathbf{Z} = \{Z(\mathbf{s}_1), \dots, Z(\mathbf{s}_D)\}^\top$ as

$$\mathbf{Z} = \max(\mathbf{0}, \max_{i=1,2,\dots} \mathbf{X}_i) = \max_{i=1,2,\dots} \mathbf{X}_i, \quad (12)$$

where the maximum is taken componentwise. The right-most equality in (12) follows from the fact that Λ is infinite, i.e., $\Lambda([0, \infty]^D \setminus \{\mathbf{0}\}) = \infty$, which implies that an infinite number of Poisson points are sampled in $[0, \infty]^D \setminus \{\mathbf{0}\}$, and that the lower boundary $\mathbf{0}$ in (12) does not contribute to the maximum. From the spectral representation (12), combined with (11), we can check that we indeed recover the expression for our max-id model in (9):

$$\begin{aligned} \Pr\{Z(\mathbf{s}_1) \leq z_1, \dots, Z(\mathbf{s}_D) \leq z_D\} &= \Pr(X_{i,1} \leq z_1, \dots, X_{i,D} \leq z_D, i = 1, 2, \dots) \\ &= \Pr(\text{No point } \mathbf{X}_i \text{ in } [0, \infty]^D \setminus [0, z_1] \times \dots \times [0, z_D]) \\ &= \exp(-\Lambda\{[0, \infty]^D \setminus [0, z_1] \times \dots \times [0, z_D]\}) \\ &= \exp\left(L\theta^\alpha - \sum_{l=1}^L \left[\theta + \sum_{j=1}^D \{z_j/K_l(\mathbf{s}_j)\}^{-1/\alpha}\right]^\alpha\right). \end{aligned}$$

The spectral representation (12) confirms that our model is indeed max-id; see Resnick (1987), Chapter 5, for more details on the spectral characterization of max-id random vectors. Such a characterization was recently exploited by Huser et al. (2017b) to construct alternative max-id models, which are quite flexible but much more intensive to fit than our proposed model.

2.4 Prior specification for the spatial kernels based on flexible log-Gaussian process factors

The basis functions used in Reich and Shaby (2012), constructed from Gaussian densities, are radial functions, decaying symmetrically from their knot centers. While it is possible to approximate a wide range of extremal functions by considering a large collection of Gaussian density basis functions $K_1(\mathbf{s}), \dots, K_L(\mathbf{s})$ as in (2), the resulting process is artificially non-stationary for fixed L . In this section, we propose an alternative prior for the basis functions, which allows for a parsimonious, yet flexible, stationary representation that can give insights into the predominant modes of spatial variability among of the underlying process.

More precisely, we extend the Reich and Shaby (2012) model by replacing the Dirac prior on the Gaussian density basis functions with flexible log-Gaussian process priors, which are more resemblant of natural phenomena than radial basis functions. This choice of basis functions is analogous to the construction of the Brown-Resnick process (Brown and Resnick, 1977; Kabluchko et al., 2009). Let $\tilde{K}_l(\mathbf{s})$, $l = 1, \dots, L - 1$, be i.i.d. mean-zero stationary Gaussian processes, each with exponential covariance function whose variance and range are $\delta_K^2 > 0$ and $\rho_K > 0$, respectively. We take the L th basis to be the constant function equal to the mean of the Gaussian process, i.e., $\tilde{K}_L(\mathbf{s}) = 0$ for all $\mathbf{s} \in \mathcal{S}$. To satisfy the sum-to-one constraint for each spatial location $\mathbf{s} \in \mathcal{S}$, we set

$$K_l(\mathbf{s}) = \exp\{\tilde{K}_l(\mathbf{s})\} / \sum_{l=1}^L \exp\{\tilde{K}_l(\mathbf{s})\}, \quad l = 1, \dots, L. \quad (13)$$

The variance parameter δ_K^2 controls the long-range spatial dependence of the max-id process $Z(\mathbf{s})$, with smaller values corresponding to stronger long-range dependence similarly to the Brown-Resnick process (see Davison et al., 2012). The Gaussian process range parameter ρ_K governs the short-range dependence, now with larger values corresponding to stronger short-range dependence. Dependence properties with this choice of random spatial kernels are further described in Section 2.6.

Finally, we note that [Oesting \(2018\)](#) recently gave a spectral representation of max-stable processes in terms of ℓ^p norms, which applies to the [Reich and Shaby \(2012\)](#) model. Following a nearly identical argument as given in that paper, the log-Gaussian basis model can be shown to be max-stable when $\theta = 0$ (see [Appendix D](#)).

2.5 Marginal modeling and realizations

Since monotone increasing transformations of the marginal distributions do not change the max-id or max-stable dependence structure, we allow for general GEV marginal distributions that are possibly different for each spatial location. In other words, we set $\tilde{Z}(\mathbf{s}) = \text{GEV}^{-1}[G_{\mathbf{s}}\{Z(\mathbf{s})\}; \mu(\mathbf{s}), \sigma(\mathbf{s}), \xi(\mathbf{s})]$, where $G_{\mathbf{s}}(z)$ is the marginal distribution of $Z(\mathbf{s})$, which in the case of the [Reich and Shaby \(2012\)](#) model is $G_{\mathbf{s}}(z) = \exp(-z^{-1})$, $z > 0$, and in the $\theta > 0$ case is given in [\(10\)](#), and $\text{GEV}^{-1}\{.; \mu(\mathbf{s}), \sigma(\mathbf{s}), \xi(\mathbf{s})\}$ is the quantile function for a GEV distribution with location $\mu(\mathbf{s})$, scale $\sigma(\mathbf{s}) > 0$, and shape $\xi(\mathbf{s})$. We treat $\tilde{Z}(\mathbf{s})$ as our response. In subsequent sections, Gaussian process priors are assumed for the GEV parameters $\mu(\mathbf{s})$, $\gamma(\mathbf{s}) = \log\{\sigma(\mathbf{s})\}$, and $\xi(\mathbf{s})$, and Markov chain Monte Carlo (MCMC) methods are used to draw posterior samples for this model. Details are given in [Appendix E](#).

To visualize some of the features of our model, we present some sample paths in [Figure 1](#). Realizations of $\tilde{Z}(\mathbf{s})$ on the unit square constructed using the Gaussian density ($L = 25$ evenly spaced basis functions, with standard deviation $\tau = 1/6$) and log-Gaussian process (variance $\delta_K^2 = 25$ and range $\rho_K = 3/4$) basis functions are shown in [Figure 1](#). For illustration, the realizations have standard Gumbel margins everywhere in space, i.e., $\mu(\mathbf{s}) = \xi(\mathbf{s}) = 0$ and $\sigma(\mathbf{s}) = 1$ for all $\mathbf{s} \in \mathcal{S}$. The figure illustrates the role of α in controlling the relative contribution of the nugget process, and the impact of θ on the asymptotic dependence structure. Weaker tail dependence is present in the max-id models ($\theta > 0$) than their max-stable counterparts ($\theta = 0$). Moreover, the general shapes of the Gaussian density basis model realizations appear less resemblant of natural processes than do those from the log-Gaussian process basis model.

While we have only developed the model for a single realization of the process $\tilde{Z}(\mathbf{s})$ so far, the model can easily be generalized to accommodate multiple replicates in time, which we will use in [Sections 3 and 4](#). In particular, treating time replicates of the process to be independent, we denote the maxima process observed at spatial location \mathbf{s} and time t by $\tilde{Z}_t(\mathbf{s})$, $t = 1, \dots, T$. We assume the marginal GEV parameters and basis functions do not vary in time, but allow the relative contribution of each basis function to be different for different time replicates of the process by taking the random basis coefficients to be $A_{l,t} \stackrel{\text{iid}}{\sim} \text{H}(\alpha, \alpha, \theta)$, $l = 1, \dots, L$, and $t = 1, \dots, T$.

2.6 Dependence Properties

In this section, we explore the dependence properties of the proposed max-id model. The parameter θ plays a crucial role in determining the asymptotic dependence class. [Reich and Shaby \(2012\)](#) show that $\{Z(\mathbf{s}), \mathbf{s} \in \mathcal{S}\}$ is asymptotically dependent and max-stable for $\alpha \in (0, 1)$, $\theta = 0$. However, when $\theta > 0$, this is no longer the case.

Proposition 2.2. *If $\theta > 0$, then the max-id process $\{Z(\mathbf{s}), \mathbf{s} \in \mathcal{S}\}$ defined in [Sections 2.2-2.4](#) using the log-Gaussian process basis prior in [\(13\)](#) is an asymptotically independent process.*

For a proof, see [Appendix B](#). [Figure 2](#) displays two common dependence measures, $\chi_u = \Pr[G_{\mathbf{s}_1}\{Z(\mathbf{s}_1)\} > u \mid G_{\mathbf{s}_2}\{Z(\mathbf{s}_2)\} > u]$ and $\bar{\chi}_u = \frac{2 \log \Pr[G_{\mathbf{s}_2}\{Z(\mathbf{s}_2)\} > u]}{\log \Pr[G_{\mathbf{s}_1}\{Z(\mathbf{s}_1)\} > u, G_{\mathbf{s}_2}\{Z(\mathbf{s}_2)\} > u]}$, $0 < u < 1$ ([Coles et al., 1999](#)) to illustrate the role of α and θ in controlling the dependence properties of the tail process. Although notationally we have omitted the dependence of χ_u on \mathbf{s}_1 and \mathbf{s}_2 , χ_u will also depend on the locations in the (non-stationary) Gaussian density basis case. Nevertheless, while χ_u is non-stationary for the [Reich and Shaby \(2012\)](#) model, it is approximately stationary

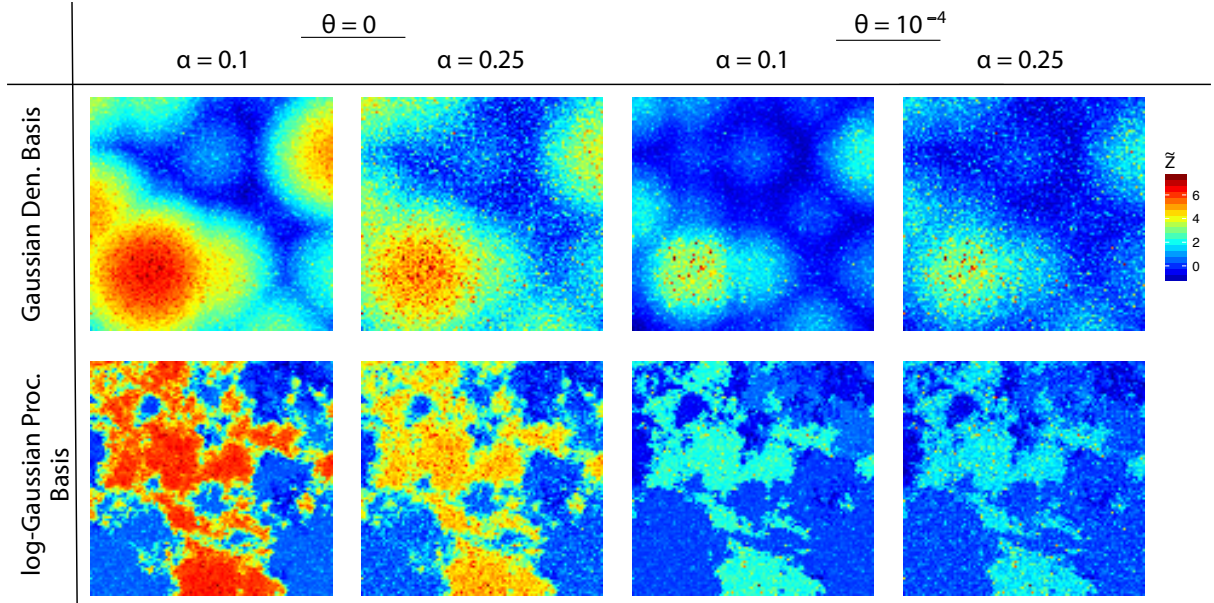


Figure 1: Realizations of the max-stable ($\theta = 0$) and max-id ($\theta > 0$) processes with Gaussian density (top) and log-Gaussian process (bottom) basis functions, plotted on Gumbel margins.

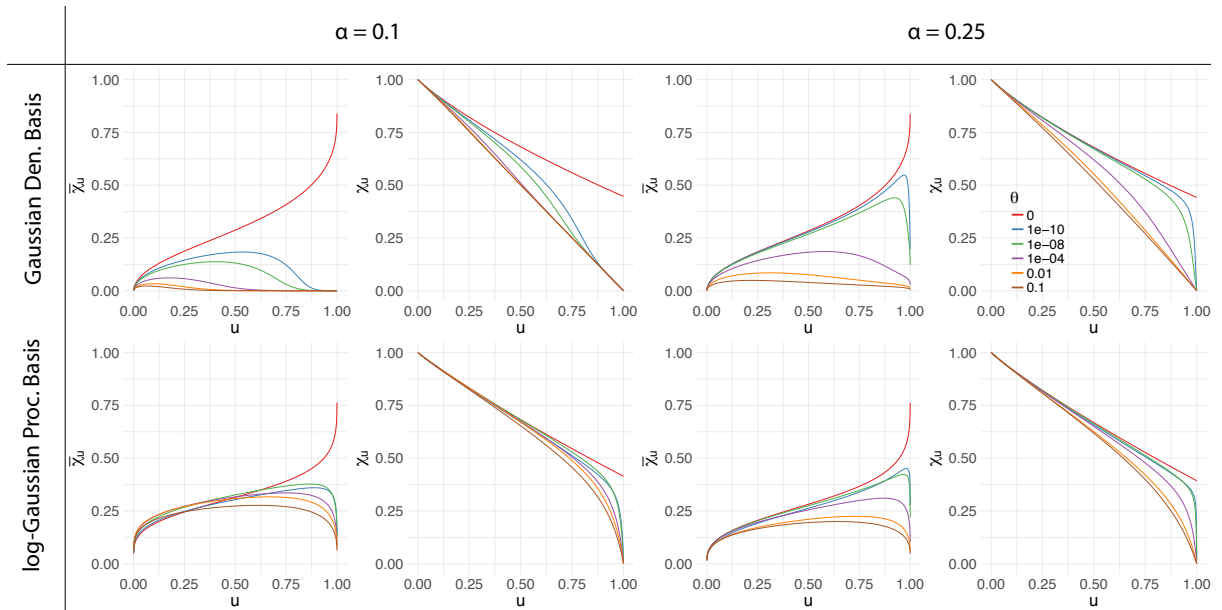


Figure 2: Dependence measures $\bar{\chi}_u$ and χ_u for the max-stable ($\theta = 0$) and max-id ($\theta > 0$) models for $Z(s)$, $s \in \mathbb{R}$, using Gaussian density ($\tau = 1/6$) and log-Gaussian process ($\delta_K^2 = 25$, $\rho_K = 3/4$) basis functions for $s_1 = 0$ and $s_2 = 1/4$. The knots ($L = 5$) of the Gaussian density basis functions are evenly spaced between 0 and 1.

for a dense set of spatial knots. An attractive feature of the proposed model is that as $\theta \downarrow 0$, χ_u and $\bar{\chi}_u$ transition smoothly from weak dependence to strong dependence for all $u < 1$.

The extremal coefficient $\theta_{\mathcal{D}}$, studied by [Schlather and Tawn \(2003\)](#), is a measure of spatial dependence along the diagonal of the finite-dimensional distributions of max-stable processes. It takes on values from $\theta_{\mathcal{D}} = 1$ when the components are perfectly dependent to $\theta_{\mathcal{D}} = D$ when they are independent, and therefore can be interpreted as the effective number of independent

Table 1: Dependence parameter simulation settings used for the Gaussian density and log-Gaussian process models.

Sim. #	1	2	3	4	5	6
α	0.1	0.25	0.1	0.25	0.1	0.25
θ	0	0	10^{-4}	10^{-4}	0.1	0.1

variables. The finite-dimensional distributions of a max-stable process with unit-Fréchet margins at level z can be written in the form

$$\Pr \{Z(\mathbf{s}_1) \leq z, \dots, Z(\mathbf{s}_D) \leq z\} = \exp \left\{ -\frac{\theta_{\mathcal{D}}(\mathbf{s}_1, \dots, \mathbf{s}_D)}{z} \right\}, \quad \theta_{\mathcal{D}}(\mathbf{s}_1, \dots, \mathbf{s}_D) \in [1, D], \quad (14)$$

where $\theta_{\mathcal{D}}$ determines the spatial dependence and does *not* depend on the level z . The rigidity of the spatial dependence structure across all quantiles limits the applicability of max-stable models to processes that exhibit varying spatial dependence types at different quantiles. From (9), we can see that the max-id extension of the Reich and Shaby (2012) model does not possess this property for $\theta > 0$.

Figure 3 contrasts the spatial dependence features of the proposed models. We examine how the conditional probability of jointly exceeding a fixed quantile decays with increasing distance. Each panel shows the spatial decay of χ_u as a function of increasing spatial lag h for several quantiles. We see a qualitatively different behavior in the spatial decay of dependence at different quantiles between the max-stable and max-id models. In the max-stable cases, the conditional exceedance probability χ_u at short spatial lags h is very similar at all levels of the distribution u . The max-id models allow for more flexibility in this respect, as can be seen by the attenuated curves for higher quantiles and wider array of spatial decay types. From Figure 3, it can be seen that for $\theta > 0$, the parameter α plays a role in how precipitous the decay in spatial dependence is with increasing distance, with smaller α corresponding to steeper decay.

3 Simulation Study

To confirm that our MCMC algorithm produces reliable results, and to evaluate the algorithm’s ability to infer the parameters of the process under different regimes, we conduct a simulation study for both the Gaussian density basis and the log-Gaussian process basis models. In all designs considered, we simulate $T = 30$ i.i.d. replicates (e.g., years) of the max-id process $\tilde{Z}(\mathbf{s})$ (defined in Section 2) observed at $N = 100$ locations uniformly distributed on the unit square $[0, 1] \times [0, 1]$. In this section only, we replace the Gaussian process priors on the GEV parameters with simpler non-spatially varying priors, as the computational burden is already quite high without spatially varying margins, and instead we use $N(0, 100)$ priors for $\mu, \gamma \equiv \log(\sigma)$, and ξ . For all simulations, data are generated using $\mu = 0$, $\sigma = 1$, and $\xi = 0$ (i.e., with standard Gumbel margins). For the Gaussian density basis model, we consider $L = 25$ knots evenly distributed over the unit square using a standard deviation of $\tau = 1/6$, and for the log-Gaussian process basis model, we use $L = 15$ basis functions and take the variance and range parameters of the underlying Gaussian processes to be $\delta_K^2 = 25$ and $\rho_K = 3/4$. We vary the settings of the dependence parameters α and θ as described in Table 1. For each simulation design, models are fitted to 100 datasets using MCMC (details are given in Appendix E). The effective sample sizes (ESS) and effective samples per second (ES/sec) for each design are reported in Appendix E.2.

The coverages of Bayesian 95% highest posterior density (HPD) credible intervals, bias, and root mean square error (RMSE) of the posterior mean estimates for the Gaussian density and log-Gaussian process basis models are reported in Tables 2 and 3, respectively. The simulation results show nearly nominal coverages in all cases. The slight positive bias of δ_K^2 and ρ_K relative

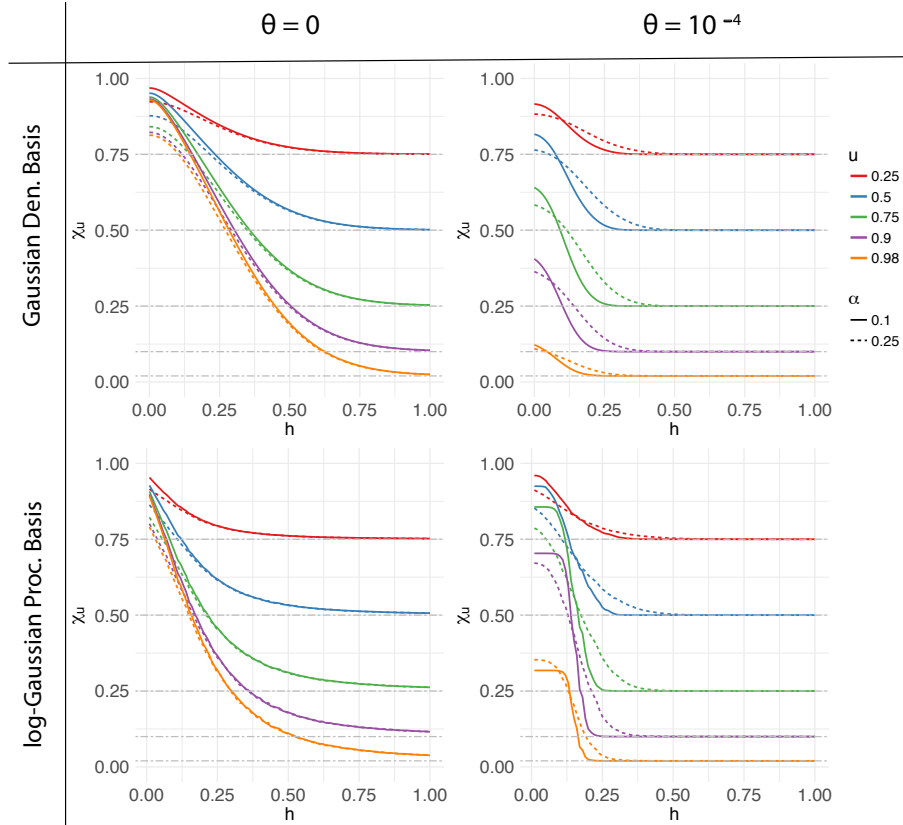


Figure 3: Dependence measure $\chi_u(h)$ between $Z(s_0)$ and $Z(s_0 + h)$ for $s_0 = 0$ as a function of h for max-stable (left column) and max-id (right column) models on $\mathcal{S} = [0, 1]$, with $L = 25$ Gaussian density basis functions with $\tau = 1/6$ (top row) and $L = 15$ log-Gaussian process basis functions with $\delta_K^2 = 25$ and $\rho_K = 3/4$ (bottom row) basis functions for varying α and u . Gaussian density basis functions are evenly spaced between 0 and 1. Estimates of $\chi_u(h)$ in the log-Gaussian process basis model are based on 50,000 Monte Carlo replicates. Horizontal dash-dot gray lines representing the values of χ_u for independent $Z(s_0)$ and $Z(s_0 + h)$ are plotted for reference.

to their magnitudes, but nominal coverage of the 95% credible intervals, suggests that these two parameters may not always be completely identifiable in practice. However, since we are more concerned with making inference on the quantiles and general spatial patterns of extremes, this is not a major concern.

4 Application to Extreme Precipitation

4.1 Data and motivation

In this section, we apply our model to extreme precipitation over the northeastern United States and Canada. Our aim is twofold: (a) to understand the spatial dependence of extreme precipitation while accounting for measurement uncertainty, and (b) to predict precipitation-induced flood-risk. The data for this application were obtained from https://hdsc.nws.noaa.gov/hdsc/pfds/pfds_series.html, which is maintained by the National Oceanic and Atmospheric Administration (NOAA). Observations consist of annual maximum daily precipitation accumulations (in inches) observed between 1960 and 2015 at $N = 646$ gauge stations (see Figure 4). The observation at gauge location \mathbf{s}_i , $i = 1, \dots, 646$, and year $t = 1, \dots, 56$, is denoted by $\tilde{Z}_t(\mathbf{s}_i)$.

Table 2: Bias, root mean squared error, and 95% credible interval coverages for parameters of Gaussian density basis models.

	α	θ	τ	μ	σ	ξ
Bias						
Sim. 1	0.0005		-0.00006	-0.006	-0.0009	0.000003
Sim. 2	0.002		-0.0003	-0.003	-0.005	0.0002
Sim. 3	0.0003	0.0001	0.0009	-0.005	0.001	-0.002
Sim. 4	-0.003	0.00003	0.002	0.004	0.003	-0.0002
Sim. 5	0.004	0.001	-0.002	-0.01	0.0005	0.003
Sim. 6	0.01	0.02	-0.002	-0.001	-0.001	0.002
RMSE						
Sim. 1	0.002		0.001	0.06	0.02	0.002
Sim. 2	0.009		0.003	0.07	0.03	0.006
Sim. 3	0.007	0.0003	0.006	0.04	0.02	0.01
Sim. 4	0.02	0.00007	0.009	0.06	0.03	0.02
Sim. 5	0.007	0.05	0.005	0.04	0.01	0.01
Sim. 6	0.03	0.06	0.01	0.05	0.02	0.01
Coverage						
Sim. 1	0.93		0.97	0.91	0.96	0.94
Sim. 2	0.97		0.94	0.96	0.97	0.94
Sim. 3	0.95	0.93	0.94	0.94	0.94	0.96
Sim. 4	0.91	0.96	0.95	0.94	0.92	0.91
Sim. 5	0.96	0.89	0.98	0.97	0.96	0.94
Sim. 6	0.94	0.94	0.94	0.93	0.96	0.96

4.2 Model fitting and validation

The precipitation data are analyzed by applying the four max-id models described in Section 2, namely (M1) Gaussian density basis, $\theta = 0$; (M2) Gaussian density basis, $\theta > 0$; (M3) log-Gaussian process basis, $\theta = 0$; and (M4) log-Gaussian process basis, $\theta > 0$, where realizations of the process for each year are treated as i.i.d. replicates. In particular, both the dependence model and GEV marginal distributions are assumed to be stationary in time. We assume independent Gaussian process priors, each with constant mean $\beta_\psi \sim N(0, 100)$ and stationary exponential covariance function $C(h) = \delta_\psi^2 \exp(-h/\rho_\psi)$, $\psi \in \{\mu, \gamma\}$, on the location $\mu(\mathbf{s})$ and log-scale $\gamma(\mathbf{s}) \equiv \log\{\sigma(\mathbf{s})\}$ marginal parameters of the GEV distribution, with half-normal priors for $\delta_\psi^2 \sim N_+(0, 100)$ and $\rho_\psi \sim N_+(0, \max_{i,j}(\|\mathbf{s}_i - \mathbf{s}_j\|)^2)$. Due to the difficulty in estimating the shape parameter (Cooley et al., 2007; Opitz et al., 2018), we use a spatially constant prior, $\xi \sim N(0, 100)$. The dependence parameter priors are as follows: For α and θ , we take $\alpha \sim \text{Unif}(0, 1)$ and $\theta \sim N_+(0, 100)$. For the Gaussian density basis models, we use $L = 60$ knot locations on an evenly spaced grid (see Figure 4). A half normal prior was put on the Gaussian density bandwidth parameter $\tau \sim N_+(0, \max_{i,j}(\|\mathbf{s}_i - \mathbf{s}_j\|)^2)$. In the case of the log-Gaussian process basis models, we use $L = 15$ basis functions, putting priors $\delta_K^2 \sim N_+(0, 100)$ and $\rho_K \sim N_+(0, \max_{i,j}(\|\mathbf{s}_i - \mathbf{s}_j\|)^2)$ on the exponential covariance parameters. Handling missing values is straightforward using the proposed approach. For each iteration of the MCMC algorithm, missing values are sampled from the posterior predictive distribution; this is detailed in Appendix F. We run each MCMC chain under two different parameter initializations for 40,000 iterations using a burn-in of 10,000 with data from 546 stations, reserving 100 stations for model evaluation. In all four cases, the posterior densities were similar across the two initializations.

Table 3: Bias, root mean squared error, and 95% credible interval coverages for parameters of log-Gaussian process basis models.

	α	θ	δ_K^2	ρ_K	μ	σ	ξ
Bias							
Sim. 1	-0.00003		2.2	0.06	0.006	-0.0004	-0.0003
Sim. 2	0.002		3.7	0.09	-0.0004	-0.002	0.0007
Sim. 3	0.0009	0.0001	2.7	0.08	-0.002	-0.001	-0.001
Sim. 4	0.002	0.00002	4.5	0.07	0.007	0.0004	0.002
Sim. 5	0.001	0.005	2.7	0.06	-0.02	-0.0005	0.002
Sim. 6	0.003	0.03	5.8	0.07	-0.005	-0.003	0.0006
RMSE							
Sim. 1	0.002		4.5	0.14	0.06	0.007	0.004
Sim. 2	0.006		5.8	0.15	0.08	0.02	0.008
Sim. 3	0.004	0.0003	5.1	0.16	0.07	0.01	0.01
Sim. 4	0.009	0.00007	7.2	0.14	0.08	0.02	0.02
Sim. 5	0.005	0.06	5.0	0.14	0.07	0.02	0.01
Sim. 6	0.02	0.06	8.7	0.15	0.06	0.03	0.02
Coverage							
Sim. 1	0.91		0.95	0.91	0.93	0.97	0.91
Sim. 2	0.93		0.93	0.92	0.95	0.98	0.96
Sim. 3	0.96	0.94	0.96	0.89	0.86	0.94	0.92
Sim. 4	0.95	0.94	0.97	0.99	0.93	0.93	0.95
Sim. 5	0.94	0.93	0.97	0.94	0.90	0.94	0.96
Sim. 6	0.93	0.93	0.92	0.93	0.95	0.95	0.95

To compare models, we calculate out-of-sample log-scores (Gneiting and Raftery, 2007), for annual maxima at the 100 holdout stations, which is simply the log-likelihood of the holdout data for each model based on conditional predictive simulations of the latent model parameters at the unobserved sites. Since the log-scores are calculated on holdout data, they implicitly account for model complexity. We also emphasize that because the predictions are based on the joint likelihood, the log-scores reflect not only the marginal fits, but also how well the model captures the dependence characteristics of the observed data. The best log-score (higher scores are better) of the two initializations for each model is reported in Table 4. The max-id models ($\theta > 0$) outperform their max-stable counterparts ($\theta = 0$). In particular, the max-id log-Gaussian process basis model with $\theta > 0$ has the highest log-score (shown in bold), suggesting it should be preferred among the considered models for this data application, and as such we focus on this model for the remainder of our analysis. For this model, the posterior mean (95% credible interval) estimates of the residual dependence parameters are 0.728 (0.703, 0.750) for α , 0.053 (0.027, 0.092) for θ , and for the spatial basis functions 35.9 (23.3, 50.5) for δ_K^2 and 520 (332, 729) miles for ρ_K , suggesting the presence of some residual dependence. Since the dependence properties of our model are smooth in θ at zero, the fact that the 95% credible interval for θ is relatively symmetric and distant from 0 gives support for asymptotic independence among precipitation extremes.

Further, to examine the model fit, we compare empirical and model-based estimates of χ_u as a function of spatial lag h and threshold u for the holdout stations (Figure 5). The left panel shows χ_u as a function of u for at fixed lags $h = 20, 100, 180, 260$ miles, and the right panel shows the spatial decay of χ_u as a function of spatial lag h for several fixed marginal quantiles

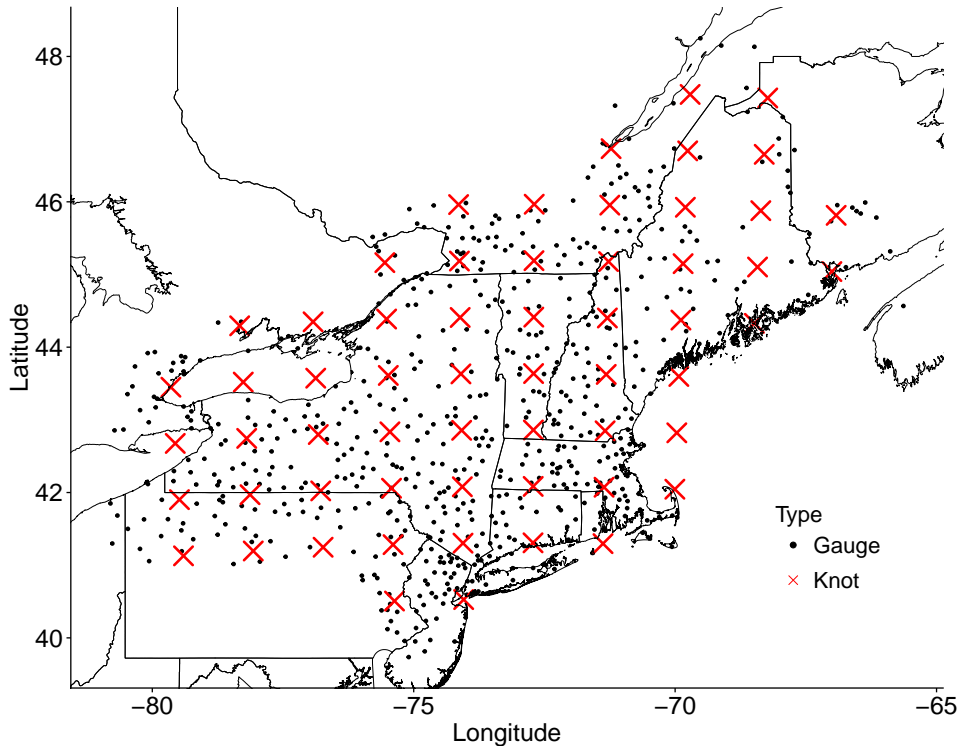


Figure 4: Precipitation gauge locations ($N = 646$) across the northeastern United States and Canada are plotted as black dots and Gaussian density basis knot locations ($L = 60$) are plotted as red crosses.

Table 4: Log-scores estimated from annual maxima observed at the holdout stations are used to compare the four models presented in Section 2. Higher log-scores correspond to better fit. The max-id, log-Gaussian process basis model has the highest log-score (shown in bold).

	Gaussian Density Basis	log-Gaussian Process Basis
$\theta = 0$	-5292.5	-5406.4
$\theta > 0$	-5218.3	-5172.6

$u = 0.25, 0.5, 0.75, 0.9, 0.98$. Empirical estimates are represented by solid lines and 95% credible intervals for each model by shaded ribbons. From the left panel, we can see that the max-id model captures the asymptotic independence behavior of the precipitation data quite well, except at very short distances where our model slightly underestimates the strong dependence present in the data. From the right panel, we deduce that the annual maximum precipitation data exhibit quite strong spatial dependence up to about 200 miles, with weaker spatial dependence at higher quantiles. Moreover, χ_u decays towards its independence level as a function of distance h faster at the 0.9 and 0.98 quantiles than at the 0.25 and 0.5 quantiles.

In order to assess the spatial prediction skill of our model, we display in Figure 6 quantile-quantile (QQ)-plots for group-wise summaries of the annual maxima taken over the 100 holdout stations (see Davison et al. (2012) for a similar analysis). The results show adequate correspondence between the model-based and empirical quantiles of the group-wise means, whereas the observed group-wise minima (maxima, respectively) appear to be slightly underestimated (overestimated, respectively) by the model.

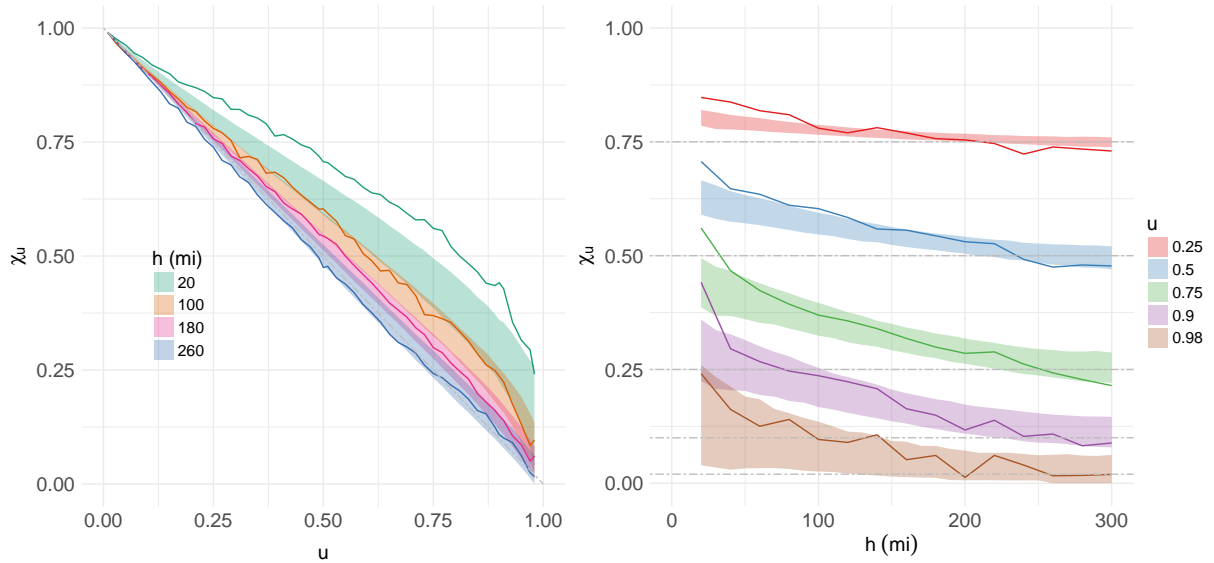


Figure 5: The left panel shows χ_u as a function of u for fixed spatial lags $h = 20, 100, 180, 260$ miles calculated for the 100-holdout stations. Empirical estimates are shown as a solid black line, and model 95% credible intervals are shown as gray ribbons. The decay of χ_u towards zero as $u \rightarrow 1$ suggests that daily precipitation are asymptotically independent. To understand the spatial dependence of extreme precipitation at increasingly extreme levels, empirical (solid lines) and model 95% credible intervals (ribbons) of $\chi_u(h)$ for the holdout stations are plotted for several quantiles $u = 0.25, 0.5, 0.75, 0.9, 0.98$ (right panel). Horizontal dash-dot gray lines representing the values of χ_u under an everywhere-independent model are plotted for reference. The plot shows good overall agreement between the model fits and empirical estimates, except at very short distances.

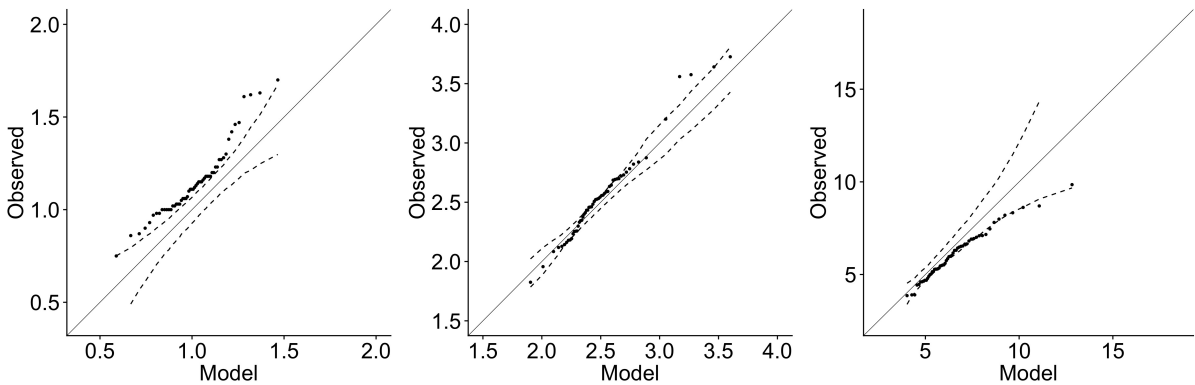


Figure 6: QQ-plots of the observed and predicted group-wise minima (left), mean (center), and maxima (right) taken over the annual maxima from all 100 holdout stations. The dashed lines represent 95% credible intervals. The plots reflect reasonable correspondence between the empirical and modeled multivariate distributions.

Maps of the marginal posterior predictive means and standard deviations of the 0.99 quantile of annual maxima (i.e., 100-year return level) for the max-id, log-Gaussian process basis model are shown in Figure 7. The posterior mean surfaces are consistent with marginal quantile surfaces for the region as reported in NOAA Atlas 14 (Perica et al., 2013). The posterior standard deviation surface shows the greatest variability in Maine, Long Island, and along the boundary

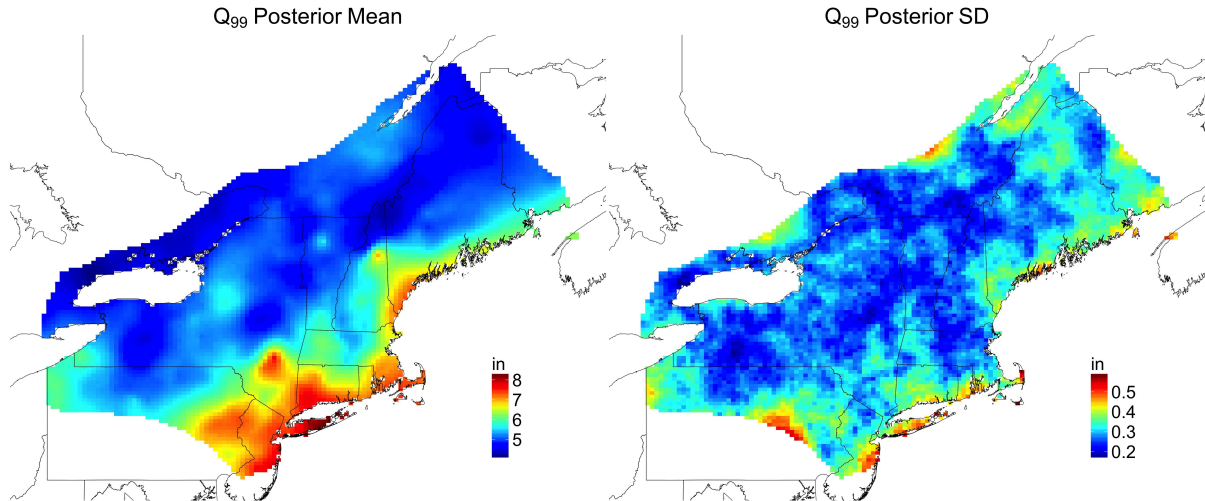


Figure 7: Pointwise posterior predictive mean (left) and standard deviation (right) of the 100-year return level of daily precipitation.

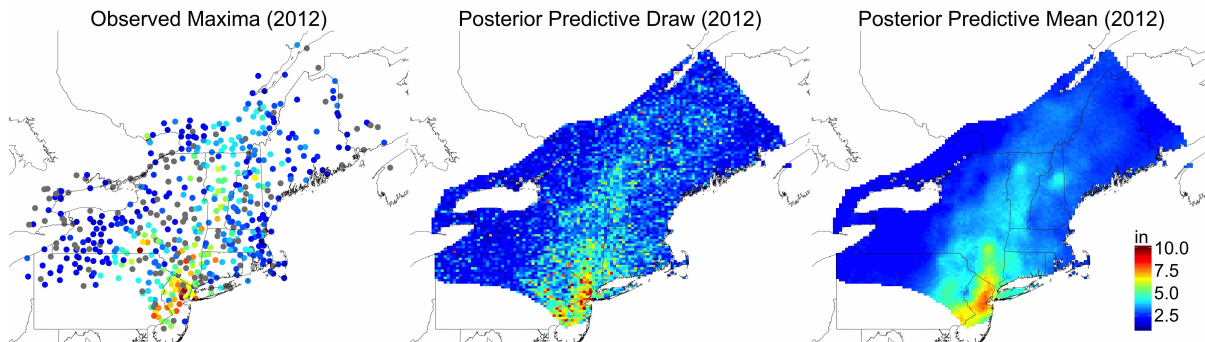


Figure 8: Observed precipitation accumulations (left), a single posterior predictive draw (middle), and posterior predictive means (right) for the year 2012. Missing values are shown in gray.

of the observation region where there are relatively few gauge locations. For illustration, observed maxima in 2012, a single posterior predictive draw, and the posterior predictive mean for that year are plotted in Figure 8. The posterior predictive plots appear to capture the general spatial characteristics of the maxima observed in 2012 well.

4.3 Analysis of the principal modes of spatial variability among precipitation extremes

Spatial principal component analysis (PCA) (Demsar et al., 2013; Jolliffe, 2002) and Empirical Orthogonal Functions (Hannachi et al., 2007) have proven to be useful methods for exploring the main large scale features of spatial processes. However, aside from recent work by Morris (2016) and Cooley and Thibaud (2016), little has been done to this end for spatial extremes. The model we have proposed allows for an exploratory visualization that is very similar to a spatial PCA method that Demsar et al. (2013) refers to as Atmospheric Science PCA in their

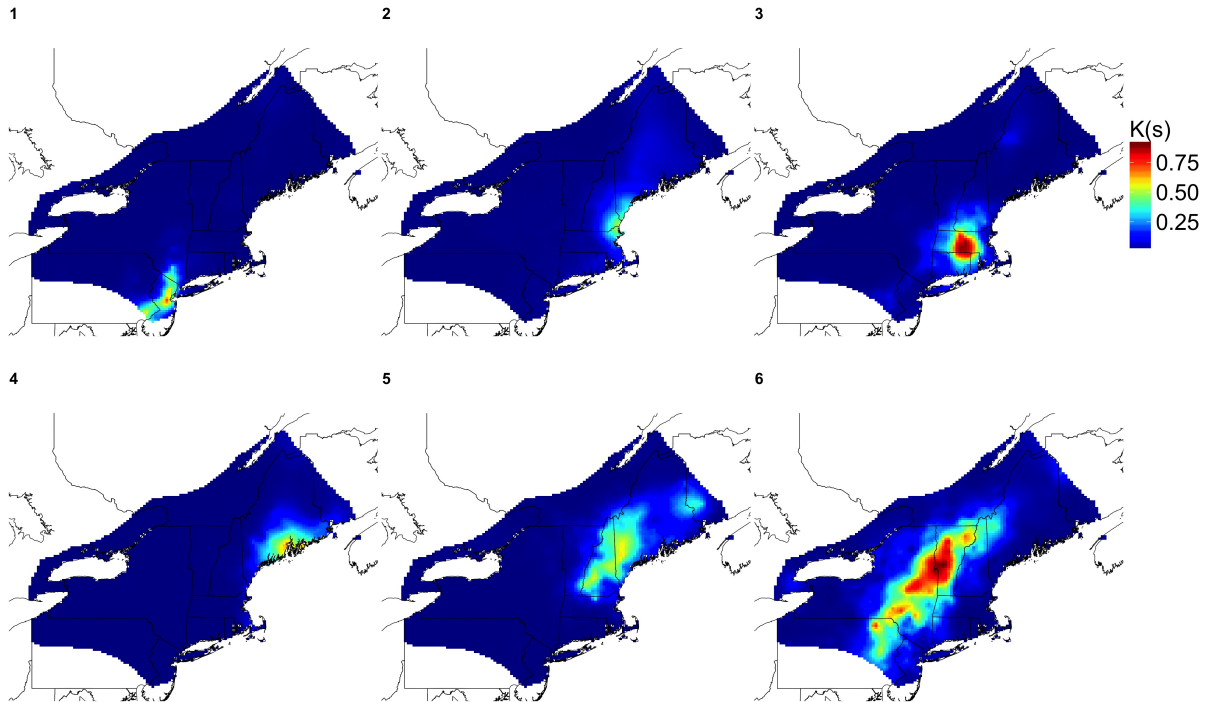


Figure 9: First six spatial basis functions ordered by the variance of their corresponding random basis coefficients from largest to smallest (left to right, top to bottom). The year-to-year variation among the coefficients of these first six basis functions accounts for 97% of the total year-to-year variation among all of the basis coefficients. The shapes of the latent factors have reasonable interpretations in terms of geographic coastal and mountain features.

review of Spatial PCA methods, where the data consist of time replicates of a univariate spatial process observed at several locations.

An attractive feature of the log-Gaussian process basis model is that it provides a low-dimensional representation of the predominant modes of spatial variability among extremes. Analogously to factor analysis, the primary spatial trends among extreme precipitation can be described by a subset of the spatial basis functions $K_l(\mathbf{s})$ that contribute the most to the overall process. To achieve this, motivated by PCA factorization, which finds the directions of maximum variance in the data, we rank the spatial basis functions $K_l(\mathbf{s})$ $l = 1, \dots, L$, by the posterior year-to-year variation of their corresponding basis coefficients $A_{l,t}$ (i.e., higher posterior variance corresponds to lower rank). Arguably, both the means and variances of the coefficients $A_{l,t}$ play a role in the relative contribution of the corresponding basis function to the overall process. However, from inspection, the basis coefficients with the highest posterior variance also have the highest posterior means. Examining the variance of the basis coefficients for each $l = 1, \dots, L$, against their ranks give a rough indication of the number of basis functions with sizable contributions to the overall process. Also, while label switching is possible, from inspection of the MCMC samples of the basis functions, this does not appear to be a major concern for this application. Posterior means of the first six spatial basis functions are shown in Figure 9.

Unlike the pointwise marginal surfaces, which do not provide any information about the joint dependence of extremes, these basis functions capture spatial regions of simultaneous (in this case, merely the same year) extreme precipitation. The proportion of the total variation among the $A_{l,t}$ accounted for by variation in the coefficients of each of the first six basis functions is 0.48, 0.33, 0.07, 0.04, 0.03, and 0.02 respectively. This does not imply that the top ranked factor

is the dominating kernel 48% of the time. Rather, if the variance of the scaling coefficients for the l th factor is high, then the year-to-year differences in the spatial modes of extremes should be well described by the peaks and troughs of the l th factor. For example, if $K_l(\mathbf{s})$ has a peak around some location \mathbf{s}^* then the conditional GEV distribution (given the factors and scaling coefficients) will be stochastically larger at \mathbf{s}^* in years when $A_{l,t}$ is large and smaller when $A_{l,t}$ is small. Therefore, the low ranked factors describe regions where precipitation tends to be extreme together or more moderate together. The latent factors in Figure 9 have reasonable physical interpretations that are reflective of natural geographic features. In particular, they resemble observed patterns in extreme precipitation events occurring along the coast and mountain range borders.

4.4 Drainage basin flood risk analysis

To understand flood-risk, it is necessary to account for the Earth’s topographic features that dictate the flow of rainwater. Drainage basins, also commonly referred to as catchment areas or watersheds, delineate a spatial region into logical hydrological units based on the natural flow of water. Precipitation falling over a single drainage basin collects into a common outlet (e.g., river, lake, or bay).

The United States is divided into increasingly granular hydrological units, each identified by a unique hydrological unit code (HUC). There are six levels to the hierarchy: regions, sub-regions, basins, sub-basins, watersheds, and sub-watersheds, each level of the hierarchy possessing a two digit code. Within a sufficiently small area, it is reasonable to assume that the pointwise maximum daily precipitation event for a single year occurs on the same day at every point, making it possible to calculate the volume of precipitation due to a single maximum precipitation event for the entire area. With this goal in mind, and in light of the long-range dependence of extreme precipitation in this region (recall Figure 5), we consider the basin (HUC6) and sub-basin (HUC8) resolutions.

The basins we consider are motivated by historical floods. In 1938, the Great New England Hurricane, one of the most powerful in recorded history, made landfall in southern New England, dropping over six inches of rainfall in some areas, and causing at that time what was the greatest amount property damage that had ever occurred due to a single storm (Brooks, 1939). For this reason, we consider Merrimack River basin covering northern Massachusetts and central New Hampshire. In addition, we also consider the Susquehanna River basins in southern New York and northeastern Pennsylvania, some of the most flood-prone areas in the country. The left panel of Figure 10 illustrates the watershed boundaries of the chosen basins.

To estimate the total volume of precipitation over a basin, we make posterior predictive draws over each sub-basin on a grid of 1 mi^2 cells by applying the prediction at the cell center uniformly over the entire cell. Specifically, denoting the prediction cell centers by $\mathbf{s}_i^*, i = 1, \dots, D^*$, each with area a , we repeat the following procedure 1,000 times for each MCMC iteration to estimate the quantiles of total precipitation volume for each basin:

- 1: With equal probability, randomly select one of the observation years, $t = 1, \dots, T$.
- 2: Draw $\tilde{Z}_t(\mathbf{s}_i^*)$ for $i = 1, \dots, D^*$, from the posterior predictive distribution.
- 3: Estimate the total volume of precipitation over the basin by $a \sum_{i=1}^{D^*} \tilde{Z}_t(\mathbf{s}_i^*)$.

Estimated survivor curves of the annual maximum total daily precipitation volume are shown in Figure 10. The right panels show estimates the total precipitation volume survivor curves, and the middle panels show the total volume estimates normalized by the total area of each sub-basin to give a measure of the flood risk relative to the size of the basin. The information from this analysis gives a sense of the flood risk due to annual precipitation events occurring on a single day. An infrastructure planner can use such estimates of the N -year return level of maximum precipitation volume (a level exceeded on average once every N years) directly to incorporate flood risk into their design requirements. The N -year return level corresponds to

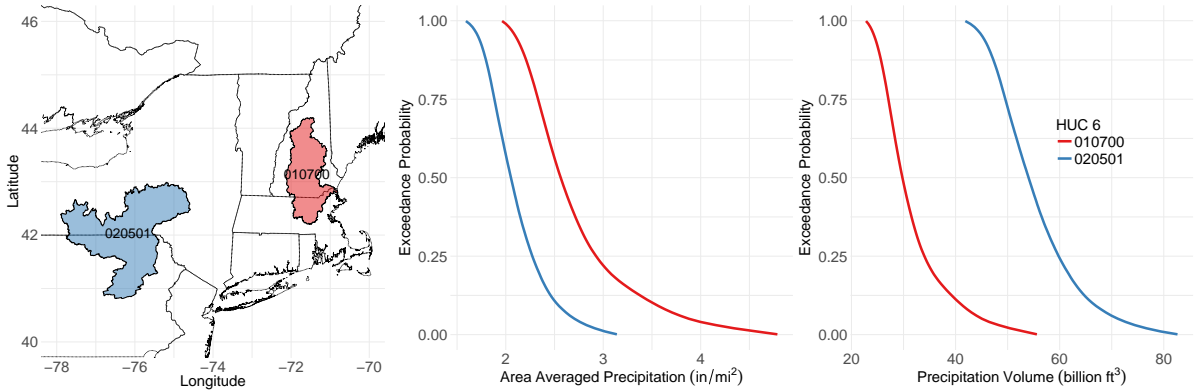


Figure 10: Merrimack River (red) and Susquehanna River (blue) basins and estimated survivor curves of the total daily precipitation volume. The middle column shows area averaged, pointwise estimates, which are calculated by dividing the total predicted basin precipitation volume by the basin area.

the $(1 - 1/N)$ th quantile of annual maximum precipitation volume. We see that the Merrimack River basin, while having a stochastically smaller estimated distribution for total precipitation volume has a stochastically larger distribution once it is normalized by basin size. We perform the same analysis for all of the sub-basins of the Merrimack River and Susquehanna River basins (Figure 11), where the assumption of simultaneous annual maxima across the entire area is even more convincing. The sub-basin survivor curves give a more granular assessment of the flood risk of the local tributaries of the main rivers. The estimated 10, 30, and 50-year return-levels for the area averaged precipitation (in/mi^2) and total precipitation volume (ft^3) are reported in Table 5.

5 Discussion

In this paper, we extend the max-stable model for spatial extremes developed by Reich and Shaby (2012) in several ways. First, by using flexible log-Gaussian process basis functions, our model provides a low-dimensional factor representation that can be used to visualize the main modes of spatial variability among extremes. Second, our approach relaxes the rigid spatial dependence structure imposed by max-stable models, while possessing the positive dependence inherent to distributions for maxima. Inference on the tail dependence class is also possible, as our model can capture asymptotic independence when $\theta > 0$, while having an asymptotically dependent, max-stable model on the boundary of the parameter space (when $\theta = 0$).

We apply our model to extreme precipitation over the northeastern United States and Canada. Because it accounts for the spatial dependence among maxima and we are able to efficiently make conditional draws from our fitted model, it is possible to estimate total precipitation volume survivor curves for annual maxima over hydrologically defined sub-basins. The precipitation predictions from our model could be incorporated into a hydrological model for the flow path dynamics that incorporates factors like drainage basin topography, land use, and land cover to describe how precipitation falling over a common catchment translates into drainage and potential flooding. The precipitation analysis does not account for the cumulative effect of heavy precipitation over several days, which can overload an urban stormwater drainage system that is already operating at capacity. Further temporal modeling of the marginal distributions and space-time dependence characteristics would facilitate such an analysis; see, e.g., Huser and Davison (2014) for space-time modeling of precipitation extremes using max-stable processes.

For future work, adding a point mass at $\theta = 0$ in the prior and proposal distributions

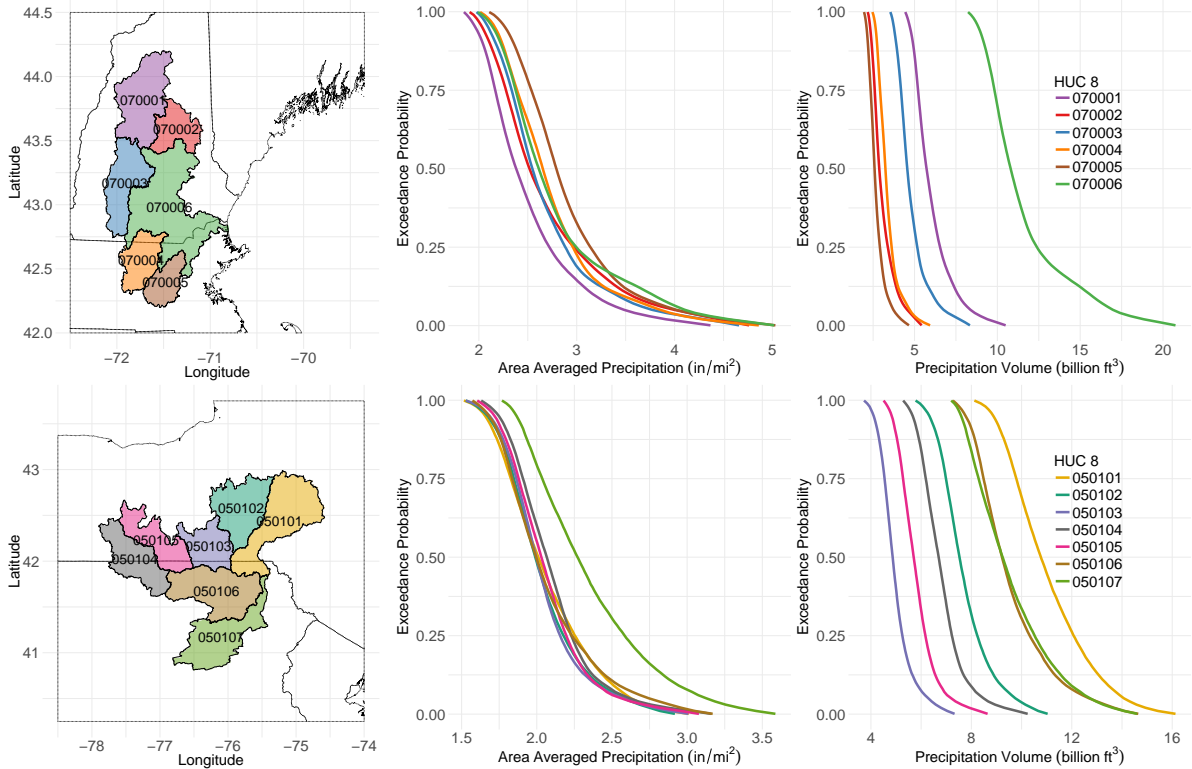


Figure 11: Merrimack River (top-left) and Susquehanna River (bottom-left) sub-basins and estimated survivor curves of the total daily precipitation volume. The middle column shows area averaged, pointwise estimates, which are calculated by dividing the total predicted sub-basin precipitation volume by the sub-basin area. The first two digits of the eight digit Hydrological Unit Code (HUC) identify the region (top: New England (01) and bottom: Mid-Atlantic (02)) and have been omitted for readability.

would make it possible to account for model uncertainty and simultaneously perform model selection directly within the MCMC. Moreover, an interesting extension of the model described here might be to assume heavier tailed distribution for the random scaling factors, such that the resulting process is asymptotically dependent, while possibly losing the max-id property. Finally, while our focus in this paper has been on flexible sub-asymptotic modeling of maxima, another avenue for research is to investigate relaxing the rigid dependence structure of limiting generalized Pareto process models for peaks-over-threshold data (see, e.g., [Castro Camilo and Huser, 2017](#); [Huser and Wadsworth, 2018](#)).

A The Generalized Extreme-Value distribution

The Generalized Extreme-Value (GEV) distribution is a limiting family for univariate block maxima, and is parameterized by a location μ , scale $\sigma > 0$, and shape ξ parameters. The distribution function for $Z \sim \text{GEV}(\mu, \sigma, \xi)$ is given by

$$G(z) = \begin{cases} \exp[-\exp\{-(z - \mu)/\sigma\}], & \xi = 0, \\ \exp[-\{1 + \xi(z - \mu)/\sigma\}_+^{-1/\xi}], & \xi \neq 0, \end{cases} \quad (15)$$

where $a_+ = \max(0, a)$, for some the location $\mu \in \mathbb{R}$, scale $\sigma > 0$, and shape $\xi \in \mathbb{R}$ parameters. In the case of $\xi \neq 0$, the support is over $\{z : 1 + \xi(z - \mu)/\sigma > 0\}$. For $\xi = 0$, the support is over \mathbb{R} .

Table 5: Area averaged precipitation (in/mi²) and total precipitation volume (billion ft³) return-level estimates for 10, 30, and 50-year return-periods are reported for the Merrimack and Susquehanna basins and sub-basins.

Basin/Sub-basin	Area Avg. Precipitation (in/mi ²)			Precipitation Volume (billion ft ³)		
	10-year	30-year	50-year	10-year	30-year	50-year
HUC 6						
010700	3.52	4.12	4.35	40.85	47.82	50.53
020501	2.52	2.81	2.92	66.35	73.98	76.74
HUC 8						
01070001	3.17	3.70	3.92	7.62	8.89	9.42
01070002	3.54	4.26	4.46	4.03	4.86	5.09
01070003	3.39	4.06	4.31	6.08	7.27	7.72
01070004	3.44	4.06	4.29	4.20	4.96	5.24
01070005	3.60	4.28	4.52	3.34	3.96	4.19
01070006	3.77	4.32	4.56	15.58	17.87	18.87
02050101	2.49	2.71	2.79	13.35	14.51	14.95
02050102	2.41	2.67	2.75	9.10	10.10	10.41
02050103	2.38	2.68	2.79	5.80	6.54	6.80
02050104	2.43	2.74	2.88	7.88	8.87	9.33
02050105	2.39	2.69	2.82	6.71	7.55	7.93
02050106	2.52	2.87	2.96	11.65	13.25	13.69
02050107	2.91	3.24	3.35	11.86	13.17	13.63

B Asymptotic independence of the max-id model

Since the marginal distributions of $Z(\mathbf{s})$ are the same when constructed using the log-Gaussian process basis, $Z(\mathbf{s}_1)$ and $Z(\mathbf{s}_2)$ are asymptotically independent if $\Pr\{Z(\mathbf{s}_1) > z | Z(\mathbf{s}_2) > z\} \rightarrow 0$ as $z \rightarrow \infty$. The marginal distribution of the process at location \mathbf{s} conditional on the basis functions is

$$G_{\mathbf{s}}\{z | K_l(\mathbf{s}), l = 1, \dots, L\} = \exp\left(L\theta^\alpha - \sum_{l=1}^L \left[\theta + \left\{\frac{K_l(\mathbf{s})}{z}\right\}^{1/\alpha}\right]^\alpha\right),$$

and the joint distribution at two locations \mathbf{s}_1 and \mathbf{s}_2 is

$$\Pr\{Z(\mathbf{s}_1) \leq z_1, Z(\mathbf{s}_2) \leq z_2 | K_l(\mathbf{s}), l = 1, \dots, L\} = \exp\left(L\theta^\alpha - \sum_{l=1}^L \left[\theta + \left\{\frac{K_l(\mathbf{s}_1)}{z_1}\right\}^{1/\alpha} + \left\{\frac{K_l(\mathbf{s}_2)}{z_2}\right\}^{1/\alpha}\right]^\alpha\right).$$

For brevity, we will drop the indices $l = 1, \dots, L$, and write, e.g., $G_{\mathbf{s}}\{z | K_l(\mathbf{s})\} \equiv G_{\mathbf{s}}\{z | K_l(\mathbf{s}), l = 1, \dots, L\}$. We have that $\lim_{z \rightarrow \infty} 1 - G_{\mathbf{s}_1}\{z | K_l(\mathbf{s})\} - G_{\mathbf{s}_2}\{z | K_l(\mathbf{s})\} + \Pr\{Z(\mathbf{s}_1) \leq z, Z(\mathbf{s}_2) \leq z | K_l(\mathbf{s})\} = 0$, and $\lim_{z \rightarrow \infty} 1 - G_{\mathbf{s}_2}\{z | K_l(\mathbf{s})\} = 0$. Thus, by *L'Hospital's rule*, we obtain

$$\begin{aligned} \chi(\mathbf{s}_1, \mathbf{s}_2) | K_l(\mathbf{s}) &= \lim_{z \rightarrow \infty} \Pr\{Z(\mathbf{s}_1) > z | Z(\mathbf{s}_2) > z, K_l(\mathbf{s})\} \\ &= \lim_{z \rightarrow \infty} \frac{1 - G_{\mathbf{s}_1}\{z | K_l(\mathbf{s})\} - G_{\mathbf{s}_2}\{z | K_l(\mathbf{s})\} + \Pr\{Z(\mathbf{s}_1) \leq z, Z(\mathbf{s}_2) \leq z | K_l(\mathbf{s})\}}{1 - G_{\mathbf{s}_2}\{z | K_l(\mathbf{s})\}} \\ &= \lim_{z \rightarrow \infty} \frac{\frac{d}{dz}[1 - G_{\mathbf{s}_1}\{z | K_l(\mathbf{s})\} - G_{\mathbf{s}_2}\{z | K_l(\mathbf{s})\} + \Pr\{Z(\mathbf{s}_1) \leq z, Z(\mathbf{s}_2) \leq z | K_l(\mathbf{s})\}]}{\frac{d}{dz}[1 - G_{\mathbf{s}_2}\{z | K_l(\mathbf{s})\}]} \\ &= 1 + \lim_{z \rightarrow \infty} \frac{\frac{d}{dz} G_{\mathbf{s}_1}\{z | K_l(\mathbf{s})\}}{\frac{d}{dz} G_{\mathbf{s}_2}\{z | K_l(\mathbf{s})\}} - \lim_{z \rightarrow \infty} \frac{\frac{d}{dz} \Pr\{Z(\mathbf{s}_1) \leq z, Z(\mathbf{s}_2) \leq z | K_l(\mathbf{s})\}}{\frac{d}{dz} G_{\mathbf{s}_2}\{z | K_l(\mathbf{s})\}}. \end{aligned} \quad (16)$$

Now for $\theta > 0$, the second term in (16) becomes

$$\begin{aligned}
\lim_{z \rightarrow \infty} \frac{\frac{d}{dz} G_{\mathbf{s}_1}\{z|K_l(\mathbf{s})\}}{\frac{d}{dz} G_{\mathbf{s}_2}\{z|K_l(\mathbf{s})\}} &= \lim_{z \rightarrow \infty} \frac{G_{\mathbf{s}_1}\{z|K_l(\mathbf{s})\} \left(\alpha z^{-(1+1/\alpha)} \sum_{l=1}^L \left[\theta + \left\{ \frac{K_l(\mathbf{s}_1)}{z} \right\}^{1/\alpha} \right]^{\alpha-1} K_l(\mathbf{s}_1)^{1/\alpha} \right)}{G_{\mathbf{s}_2}\{z|K_l(\mathbf{s})\} \left(\alpha z^{-(1+1/\alpha)} \sum_{l=1}^L \left[\theta + \left\{ \frac{K_l(\mathbf{s}_2)}{z} \right\}^{1/\alpha} \right]^{\alpha-1} K_l(\mathbf{s}_2)^{1/\alpha} \right)} \\
&= \lim_{z \rightarrow \infty} \frac{G_{\mathbf{s}_1}\{z|K_l(\mathbf{s})\}}{G_{\mathbf{s}_2}\{z|K_l(\mathbf{s})\}} \times \lim_{z \rightarrow \infty} \frac{\sum_{l=1}^L \left[\theta + \left\{ \frac{K_l(\mathbf{s}_1)}{z} \right\}^{1/\alpha} \right]^{\alpha-1} K_l(\mathbf{s}_1)^{1/\alpha}}{\sum_{l=1}^L \left[\theta + \left\{ \frac{K_l(\mathbf{s}_2)}{z} \right\}^{1/\alpha} \right]^{\alpha-1} K_l(\mathbf{s}_2)^{1/\alpha}} \\
&= \frac{\sum_{l=1}^L K_l(\mathbf{s}_1)^{1/\alpha}}{\sum_{l=1}^L K_l(\mathbf{s}_2)^{1/\alpha}}, \tag{17}
\end{aligned}$$

and the third term in (16) becomes

$$\begin{aligned}
&\lim_{z \rightarrow \infty} \frac{\frac{d}{dz} \Pr\{Z(\mathbf{s}_1) \leq z, Z(\mathbf{s}_2) \leq z|K_l(\mathbf{s})\}}{\frac{d}{dz} G_{\mathbf{s}_2}\{z|K_l(\mathbf{s})\}} \\
&= \lim_{z \rightarrow \infty} \frac{\Pr\{Z(\mathbf{s}_1) \leq z, Z(\mathbf{s}_2) \leq z|K_l(\mathbf{s})\} \left(\alpha z^{-(1+1/\alpha)} \sum_{l=1}^L \left[\theta + \left\{ \frac{K_l(\mathbf{s}_1)}{z} \right\}^{1/\alpha} + \left\{ \frac{K_l(\mathbf{s}_2)}{z} \right\}^{1/\alpha} \right]^{\alpha-1} \left\{ K_l(\mathbf{s}_1)^{1/\alpha} + K_l(\mathbf{s}_2)^{1/\alpha} \right\} \right)}{G_{\mathbf{s}_2}\{z|K_l(\mathbf{s})\} \left(\alpha z^{-(1+1/\alpha)} \sum_{l=1}^L \left[\theta + \left\{ \frac{K_l(\mathbf{s}_2)}{z} \right\}^{1/\alpha} \right]^{\alpha-1} K_l(\mathbf{s}_2)^{1/\alpha} \right)} \\
&= \lim_{z \rightarrow \infty} \frac{\Pr\{Z(\mathbf{s}_1) \leq z, Z(\mathbf{s}_2) \leq z|K_l(\mathbf{s})\}}{G_{\mathbf{s}_2}\{z|K_l(\mathbf{s})\}} \lim_{z \rightarrow \infty} \frac{\sum_{l=1}^L \left[\theta + \left\{ \frac{K_l(\mathbf{s}_1)}{z} \right\}^{1/\alpha} + \left\{ \frac{K_l(\mathbf{s}_2)}{z} \right\}^{1/\alpha} \right]^{\alpha-1} \left\{ K_l(\mathbf{s}_1)^{1/\alpha} + K_l(\mathbf{s}_2)^{1/\alpha} \right\}}{\sum_{l=1}^L \left[\theta + \left\{ \frac{K_l(\mathbf{s}_2)}{z} \right\}^{1/\alpha} \right]^{\alpha-1} K_l(\mathbf{s}_2)^{1/\alpha}} \\
&= \frac{\sum_{l=1}^L K_l(\mathbf{s}_1)^{1/\alpha} + K_l(\mathbf{s}_2)^{1/\alpha}}{\sum_{l=1}^L K_l(\mathbf{s}_2)^{1/\alpha}} \\
&= 1 + \frac{\sum_{l=1}^L K_l(\mathbf{s}_1)^{1/\alpha}}{\sum_{l=1}^L K_l(\mathbf{s}_2)^{1/\alpha}}. \tag{18}
\end{aligned}$$

Combining (17) and (18) together in (16) gives $\chi(\mathbf{s}_1, \mathbf{s}_2)|K_l(\mathbf{s}) = 0$ for all $\mathbf{s}_1, \mathbf{s}_2$ when $\theta > 0$.

Finally, writing $\chi_z(\mathbf{s}_1, \mathbf{s}_2)|K_l(\mathbf{s}) = \Pr\{Z(\mathbf{s}_1) > z|Z(\mathbf{s}_2) > z, K_l(\mathbf{s})\}$, we obtain

$$\chi(\mathbf{s}_1, \mathbf{s}_2) = \lim_{z \rightarrow \infty} \chi_z(\mathbf{s}_1, \mathbf{s}_2) = \lim_{z \rightarrow \infty} \mathbb{E}\{\chi_z(\mathbf{s}_1, \mathbf{s}_2)|K_l(\mathbf{s})\} = \mathbb{E}\{\lim_{z \rightarrow \infty} \chi_z(\mathbf{s}_1, \mathbf{s}_2)|K_l(\mathbf{s})\} = 0$$

for all $\mathbf{s}_1, \mathbf{s}_2 \in \mathcal{S}$, where the second to last line follows from the Dominated Convergence Theorem since $|\chi_z(\mathbf{s}_1, \mathbf{s}_2)|K_l(\mathbf{s})| < 1$.

C Simulating Hougaard random variables

Simulating from an exponentially tilted density using a simple rejection sampler becomes increasingly difficult as the exponential tilting parameter grows. The expected number of iterations for the following simple rejection sampler grows according to $1/\mathbb{E}\{\exp(-\theta X_1)\}$ if X_1 has density f and X_2 follows an exponentially tilted f with tilting parameter $\theta > 0$:

- 1: **repeat**
- 2: Generate $X_1 \sim f$
- 3: Generate $U \sim \text{Unif}(0, 1)$
- 4: **until** $U \leq \exp(-\theta X_1)$
- 5: Set $X_2 = X_1$.

Devroye (2009) developed a fast double rejection method that is uniformly fast over all tilting parameters, which is useful when θ is large. For the proposed model, the more interesting values of θ occur when θ is small, for which the simple rejection sampler is sufficient.

D Max-stability of log-Gaussian process basis model

Recently, [Oesting \(2018\)](#) gave a spectral representation of max-stable processes in terms of ℓ^p norms, which applies to the [Reich and Shaby \(2012\)](#) model. We reproduce this theorem below for reference. See [Oesting \(2018\)](#) for a proof. Denote the ℓ^p norm of Hadamard product of sequences $\mathbf{A} = \{A_i\}_{i \in \mathbb{N}}$ and $\mathbf{W} = \{W_i(\mathbf{s})\}_{i \in \mathbb{N}}$, $\mathbf{s} \in \mathcal{S}$, by

$$\|\mathbf{A} \circ \mathbf{W}(\mathbf{s})\|_p = \begin{cases} [\sum_{i \in \mathbb{N}} \{A_i W_i(\mathbf{s})\}^p]^{1/p}, & p \in (1, \infty), \\ \max_{i \in \mathbb{N}} A_i W_i(\mathbf{s}), & p = \infty. \end{cases}$$

Theorem D.1. *Let $p \in (1, \infty]$ and $\{U(\mathbf{s})\}_{\mathbf{s} \in \mathcal{S}}$ be a collection of p -Fréchet random variables, and $\sum_{i \in \mathbb{N}} \delta_{A_i}$ be a Poisson process on $(0, \infty)$ with intensity $a^{-2} da$. If $W_i, i \in \mathbb{N}$ are independent copies of a stochastic process $\{W(\mathbf{s}), \mathbf{s} \in \mathcal{S}\}$ with $E\{W(\mathbf{s})\} = 1$ for all $\mathbf{s} \in \mathcal{S}$, then the process X , defined by*

$$X(\mathbf{s}) = \frac{U(\mathbf{s})}{\Gamma(1 - 1/p)} \|\mathbf{A} \circ \mathbf{W}(\mathbf{s})\|_p, \quad \mathbf{s} \in \mathcal{S} \quad (19)$$

is max-stable with unit Fréchet margins.

The extension of the [Reich and Shaby \(2012\)](#) model to the normalized log-Gaussian basis functions when $\theta = 0$ can be seen to be max-stable by applying [Theorem D.1](#) with $p = 1/\alpha$, and where W has discrete distribution defined by $\Pr(W = LK_l) = 1/L$, $l = 1, \dots, L$, so that $E\{W(\mathbf{s})\} = 1$ for all $\mathbf{s} \in \mathcal{S}$.

E MCMC Details

E.1 Metropolis-Hastings algorithm

We implement Metropolis-Hastings MCMC algorithms in R (<http://www.r-project.org>) to draw posterior samples for the models described in this paper. Parameters α , θ , τ , β_ψ , δ_ψ^2 , ρ_ψ , $\psi \in \{\mu, \sigma\}$, ξ , δ_K^2 , and ρ_K are all updated using variable-at-a-time Normal random walks. Scaling factors $A_{i,t}$ are updated using variable-at-a-time Normal random walks on a log-scale. From [\(8\)](#), when $\theta > 0$, the density for $A_{i,t}$ can be expressed in terms of a $\text{PS}(\alpha)$ density. The density function for the positive stable distribution is not available in closed form, but has a convenient bivariate integral representation ([Stephenson, 2009](#); [Kanter, 1975](#); [Ibragimov and Chernin, 1959](#)), which we evaluate numerically. For $\alpha \in (0, 1)$,

$$f_{\text{PS}}(x) = \int_0^1 \frac{\alpha}{1-\alpha} x^{-1/(1-\alpha)} a(\pi u) \exp\left\{-x^{-\alpha/(1-\alpha)} a(\pi u)\right\} du,$$

where

$$a(v) = \left\{ \frac{\sin(\alpha v)}{\sin(v)} \right\}^{1/(1-\alpha)} \frac{\sin\{(1-\alpha)v\}}{\sin(\alpha v)}.$$

The computational burden associated with the log-Gaussian process basis functions and GEV marginal parameter Gaussian processes is one of the limiting factors in the scaling of the proposed model to many spatial locations. Often the strong correlations in the posterior distribution of a Gaussian process at nearby spatial locations make finding an efficient proposal difficult. To address this, we adapt a common sampling scheme that uses a Cholesky decomposition of the covariance matrix to transform the highly correlated Gaussian process to an i.i.d. scale ([Kuss and Rasmussen, 2005](#)). If X is multivariate normal, $X \sim N(\mathbf{0}, \Sigma)$, then for Cholesky decomposition $\Sigma = LL^\top$, setting $Y = L^{-1}X$ gives $Y \sim N(\mathbf{0}, I)$. Performing Cholesky decompositions on large matrices at every MCMC iteration can quickly become expensive and is needless for our purposes if the range of the spatial dependence is not too large. With this in mind, we first partition our spatial region into disjoint sub-regions and perform block updates within each.

We illustrate our proposal scheme for the GEV location parameter, but the same approach applies generically to others. Without loss of generality, assume that $\{\mu(\mathbf{s}), \mathbf{s} \in \mathbb{R}^2\}$ has mean zero Gaussian process prior with exponential covariance function $C(h; \rho_\mu, \delta_\mu^2)$, of which we would like to draw posterior samples. We first apply a k -nearest-neighbors clustering algorithm on the set of observation locations $\mathbf{s}_1, \dots, \mathbf{s}_D$ to partition them into J disjoint clusters, which we fix for the remainder of the algorithm. Let $\tau(j)$ denote the set of D_j spatial indices for the j^{th} cluster. For the precipitation analysis, we take $J = 20$, however in general this choice should depend on the practical range of the process. Also, note that clustering on a spatially varying covariate instead of just the spatial locations could improve the efficiency of the sampler further.

Let $\boldsymbol{\mu}_j^{(m)} = [\mu\{\mathbf{s}_{\tau(j)_1}\}^{(m)}, \dots, \mu\{\mathbf{s}_{\tau(j)_{D_j}}\}^{(m)}]^\top$ be the m^{th} MCMC draw of the process at the D_j observation locations of the j^{th} partition, and $\Sigma_{\mu_j}^{(m)}$ the corresponding covariance matrix obtained by evaluating $C(h; \rho_\mu^{(m)}, \delta_\mu^{2(m)})$ at all pairs of observation locations in the j^{th} cluster, and L_{μ_j} its Cholesky factor. For each cluster, we perform block random-walk updates as follows:

- 1: Set $\check{\boldsymbol{\mu}}_j^{(m)} = L_{\mu_j}^{-1} \boldsymbol{\mu}_j^{(m)}$
- 2: Propose $\check{\boldsymbol{\mu}}_j^* \sim N(\check{\boldsymbol{\mu}}_j^{(m)}, \lambda_{\mu_j}^2 I)$
- 3: Set $\boldsymbol{\mu}_j^* = L_{\mu_j} \check{\boldsymbol{\mu}}_j^*$
- 4: Retain $\boldsymbol{\mu}_j^*$ with probability $R = \min\{1, f_\mu(\boldsymbol{\mu}_j^* | \Psi^{(m)}, \mathbf{z}) / f_\mu(\boldsymbol{\mu}_j^{(m)} | \Psi^{(m)}, \mathbf{z})\}$,

where f_μ is the full conditional distribution for $\boldsymbol{\mu}$ given the data \mathbf{z} and remaining parameters Ψ , and the proposal variance $\lambda_{\mu_j}^2$ can be adaptively tuned (Shaby and Wells, 2010).

The proposals for the Gaussian process basis functions are similar, but the blocking scheme also takes advantage of the dependence induced by the sum-to-one constraint. Let $\mathbf{K}_{l,j}^{(m)} = [K_l^{(m)}\{\mathbf{s}_{\tau(j)_1}\}, \dots, K_l^{(m)}\{\mathbf{s}_{\tau(j)_{D_j}}\}]^\top$, $l = 1, \dots, L$, be the m^{th} MCMC draw of the log-Gaussian process basis functions. For each spatial location \mathbf{s} , we transform the basis functions to the Gaussian process scale $\tilde{K}_l^{(m)}(\mathbf{s}) = \log \left\{ \frac{K_l^{(m)}(\mathbf{s})}{\sum_{l=1}^L K_l^{(m)}(\mathbf{s})} \right\}$, $l = 1, \dots, L$. Then, just as before denoting the prior Gaussian process covariance matrix for the j^{th} partition by the $\Sigma_{\tilde{K}_j}$ and corresponding Cholesky factor by $L_{\tilde{K}_j}$ (common across all $l = 1, \dots, L - 1$), the Metropolis update is

- 1: **for** $l = 1, \dots, L - 1$ **do**
- 2: Set $\check{\mathbf{K}}_{l,j}^{(m)} = L_{\tilde{K}_j}^{-1} \tilde{\mathbf{K}}_{l,j}^{(m)}$
- 3: Propose $\check{\mathbf{K}}_{l,j}^* \sim N(\check{\mathbf{K}}_{l,j}^{(m)}, \lambda_{K_j}^2 I)$
- 4: Set $\tilde{\mathbf{K}}_{l,j}^* = L_{\tilde{K}_j} \check{\mathbf{K}}_{l,j}^*$
- 5: **end for**
- 6: Define $K_L^*(\mathbf{s}) = 1$ for all \mathbf{s}
- 7: Set $K_l^*(\mathbf{s}_{\tau(j)_i}) = \exp \left\{ \tilde{K}_l^*(\mathbf{s}_{\tau(j)_i}) \right\} / \sum_{l=1}^L \exp \left\{ \tilde{K}_l^*(\mathbf{s}_{\tau(j)_i}) \right\}$, for $l = 1, \dots, L$, and $i = 1, \dots, D_j$
- 8: Retain $\mathbf{K}_{l,j}^*$ with probability $R = \min\{1, f_K(\mathbf{K}_{l,j}^* | \Psi^{(m)}, \mathbf{z}) / f_K(\mathbf{K}_{l,j}^{(m)} | \Psi^{(m)}, \mathbf{z})\}$,

where f_K is the full conditional distribution for $\mathbf{K}_{l,j}^* = (K_l^*(\mathbf{s}_{\tau(j)_1}), \dots, K_l^*(\mathbf{s}_{\tau(j)_{D_j}}))^\top$, $l = 1, \dots, L$.

E.2 Computation time

The average effective sample sizes (ESS), and effective samples per second (ES/sec) for the simulations described in Section 3 are reported in Tables 6 and 7. In general, the efficiency of samplers for the log-Gaussian process basis models is better than for the Gaussian density basis models due to the smaller number of $A_{l,t}$ terms. Also, samplers for the max-stable ($\theta = 0$) models are more efficient than their max-id counterparts due to the closed-form expression of the marginal quantile functions for $\tilde{Z}(\mathbf{s})$ in the max-stable case. For the max-id models, the marginal quantile functions for $\tilde{Z}(\mathbf{s})$ are obtained by numerical inversion of the distribution

Table 6: The average effective sample sizes (ESS), and effective samples per second (ES/sec) for MCMC samplers of the log-Gaussian process basis simulation study.

	α	θ	δ_K^2	ρ_K	μ	σ	ξ
ESS							
Sim. 1	123		379	378	109	227	408
Sim. 2	172		336	336	128	214	583
Sim. 3	134	118	366	365	115	413	803
Sim. 4	218	185	281	291	137	368	900
Sim. 5	121	116	340	345	123	380	1080
Sim. 6	136	128	243	262	187	434	1752
ES/sec							
Sim. 1	0.004		0.011	0.011	0.003	0.007	0.012
Sim. 2	0.005		0.010	0.010	0.004	0.007	0.018
Sim. 3	0.002	0.002	0.005	0.005	0.002	0.006	0.011
Sim. 4	0.003	0.003	0.004	0.005	0.002	0.006	0.014
Sim. 5	0.002	0.002	0.005	0.005	0.002	0.006	0.017
Sim. 6	0.002	0.002	0.004	0.004	0.003	0.007	0.028

Table 7: The average effective sample sizes (ESS), and effective samples per second (ES/sec) for MCMC samplers of the Gaussian density basis simulation study.

	α	θ	τ	μ	σ	ξ
ESS						
Sim. 1	111		138	111	135	1527
Sim. 2	121		147	131	137	1562
Sim. 3	128	114	127	145	387	1452
Sim. 4	169	183	172	174	250	553
Sim. 5	121	112	127	186	682	2859
Sim. 6	128	119	138	446	661	3308
ES/sec						
Sim. 1	0.002	0.166	0.003	0.002	0.003	0.032
Sim. 2	0.003	0.177	0.003	0.003	0.003	0.034
Sim. 3	0.001	0.001	0.001	0.001	0.003	0.013
Sim. 4	0.002	0.002	0.002	0.002	0.002	0.005
Sim. 5	0.001	0.001	0.001	0.002	0.006	0.026
Sim. 6	0.001	0.001	0.001	0.004	0.006	0.032

function.

F Posterior predictive draws

In this section we describe how to make posterior predictive draws from the proposed model. We will make use of the following fact about multivariate normal distributions: let $\mathbf{W} = (\mathbf{W}_1^\top, \mathbf{W}_2^\top)^\top$, where \mathbf{W}_1 and \mathbf{W}_2 are p and q vectors, respectively. If \mathbf{W} has multivariate normal distribution

$$\mathbf{W} \sim N \left(\begin{pmatrix} \boldsymbol{\mu}_1 \\ \boldsymbol{\mu}_2 \end{pmatrix}, \begin{pmatrix} \Sigma_{11} & \Sigma_{12} \\ \Sigma_{21} & \Sigma_{22} \end{pmatrix} \right),$$

then $\mathbf{W}_1 | \mathbf{W}_2 = \mathbf{w}_2 \sim N(\boldsymbol{\mu}_1 + \Sigma_{12}\Sigma_{22}^{-1}(\mathbf{w}_2 - \boldsymbol{\mu}_2), \Sigma_{11} - \Sigma_{12}\Sigma_{22}^{-1}\Sigma_{21})$.

Now, let m index the MCMC iteration, and let \mathbf{s}^* denote a prediction location. For each of $\mathbf{s}_1, \dots, \mathbf{s}_D$, we first transform the basis functions to the Gaussian process scale by $\tilde{K}_l^{(m)}(\mathbf{s}) = \log \left\{ \frac{K_l^{(m)}(\mathbf{s})}{\sum_{l=1}^L K_l^{(m)}(\mathbf{s})} \right\}$, $l = 1, \dots, L$. Then, for $l = 1, \dots, L - 1$, we simulate the l^{th} basis function $\tilde{K}_l^{(m)}(\mathbf{s}^*) | \tilde{K}_l^{(m)}(\mathbf{s}_1), \dots, \tilde{K}_l^{(m)}(\mathbf{s}_D), \delta^{2(m)}, \rho^{(m)}$ from the corresponding conditional multivariate normal distribution. We set $\tilde{K}_L^{(m)}(\mathbf{s}^*) = 1$, and normalize each basis function at the prediction location by $K_l^{(m)}(\mathbf{s}^*) = \exp\{\tilde{K}_l^{(m)}(\mathbf{s}^*)\} / \sum_{l=1}^L \exp\{\tilde{K}_l^{(m)}(\mathbf{s}^*)\}$, $l = 1, \dots, L$. Then, we (conditionally) simulate GEV marginal parameters at prediction location from the corresponding multivariate normal distributions (e.g., $\mu^{(m)}(\mathbf{s}^*) | \mu^{(m)}(\mathbf{s}_1), \dots, \mu^{(m)}(\mathbf{s}_D), \delta_{\mu}^{2(m)}, \rho_{\mu}^{(m)}$). Finally, we apply the following procedure to make draws of $\tilde{Z}_t^{(m)}(\mathbf{s}^*)$ from the posterior predictive distribution, for each year t ,

- 1: Set $Y_t^{(m)}(\mathbf{s}^*) = \left\{ \sum_{l=1}^L A_{l,t}^{(m)} \tilde{K}_l^{(m)}(\mathbf{s}^*)^{1/\alpha} \right\}^{\alpha^{(m)}}$;
- 2: Draw $Z_t^{(m)}(\mathbf{s}^*) | Y_t^{(m)}(\mathbf{s}^*)$, and $\alpha^{(m)} \sim \text{GEV}\{Y_t^{(m)}(\mathbf{s}^*), \alpha^{(m)} Y_t^{(m)}(\mathbf{s}^*), \alpha^{(m)}\}$;
- 3: Set $\tilde{Z}_t^{(m)}(\mathbf{s}^*) = \text{GEV}^{-1} \left[G_{\mathbf{s}^*} \left\{ Z_t^{(m)}(\mathbf{s}^*) \right\}; \mu^{(m)}(\mathbf{s}^*), \sigma^{(m)}(\mathbf{s}^*), \xi^{(m)}(\mathbf{s}^*) \right]$,

where GEV^{-1} is the GEV quantile function, and $G_{\mathbf{s}^*}$ denotes the (marginal) distribution function of $\tilde{Z}^{(m)}(\mathbf{s}^*)$.

References

- Brooks, C. F. (1939). Hurricanes into new england: meteorology of the storm of september 21, 1938. *Geographical Review* 29(1), 119–127.
- Brown, B. M. and S. I. Resnick (1977). Extreme values of independent stochastic processes. *Journal of Applied Probability* 14(4), 732–739.
- Castro Camilo, D. and R. Huser (2017). Local likelihood estimation of complex tail dependence structures in high dimensions, applied to U.S. precipitation extremes. arXiv preprint 1710.00875.
- Coles, S., J. Heffernan, and J. Tawn (1999). Dependence measures for extreme value analyses. *Extremes* 2(4), 339.
- Cooley, D., D. Nychka, and P. Naveau (2007). Bayesian spatial modeling of extreme precipitation return levels. *J. Amer. Statist. Assoc.* 102(479), 824–840.
- Cooley, D. and E. Thibaud (2016). Decompositions of dependence for high-dimensional extremes. *arXiv preprint arXiv:1612.07190*.
- Davison, A. C., R. Huser, and E. Thibaud (2013). Geostatistics of dependent and asymptotically independent extremes. *Math. Geosci.* 45(5), 511–529.
- Davison, A. C., R. Huser, and E. Thibaud (2018). Spatial extremes. In A. E. Gelfand, M. Fuentes, and R. L. Smith (Eds.), *Handbook of Environmental and Ecological Statistics*. CRC Press. (accepted).
- Davison, A. C., S. A. Padoan, and M. Ribatet (2012). Statistical modeling of spatial extremes. *Statist. Sci.* 27(2), 161–186.

- de Haan, L. and A. Ferreira (2006). *Extreme value theory*. Springer Series in Operations Research and Financial Engineering. Springer, New York. An introduction.
- Demsar, U., P. Harris, C. Brunson, A. S. Fotheringham, and S. McLoone (2013). Principal component analysis on spatial data: an overview. *Annals of the Association of American Geographers* 103(1), 106–128.
- Devroye, L. (2009). Random variate generation for exponentially and polynomially tilted stable distributions. *ACM Transactions on Modeling and Computer Simulation (TOMACS)* 19(4), 18.
- Dombry, C., F. Éyi-Minko, and M. Ribatet (2013). Conditional simulation of max-stable processes. *Biometrika* 100(1), 111–124.
- Ferreira, A. and L. de Haan (2014). The generalized Pareto process; with a view towards application and simulation. *Bernoulli* 20(4), 1717–1737.
- Fougères, A.-L., J. P. Nolan, and H. Rootzén (2009). Models for dependent extremes using stable mixtures. *Scand. J. Stat.* 36(1), 42–59.
- Gneiting, T. and A. E. Raftery (2007). Strictly proper scoring rules, prediction, and estimation. *J. Amer. Statist. Assoc.* 102(477), 359–378.
- Hannachi, A., I. Jolliffe, and D. Stephenson (2007). Empirical orthogonal functions and related techniques in atmospheric science: A review. *International journal of climatology* 27(9), 1119–1152.
- Hougaard, P. (1986). Survival models for heterogeneous populations derived from stable distributions. *Biometrika* 73(2), 387–396.
- Huser, R. and A. C. Davison (2014). Space-time modelling of extreme events. *J. R. Stat. Soc. Ser. B. Stat. Methodol.* 76(2), 439–461.
- Huser, R., T. Opitz, and E. Thibaud (2017a). Bridging asymptotic independence and dependence in spatial extremes using Gaussian scale mixtures. *Spat. Stat.* 21(part A), 166–186.
- Huser, R., T. Opitz, and E. Thibaud (2017b). Penultimate modeling of spatial extremes: statistical inference for max-infinitely divisible processes.
- Huser, R. G. and J. L. Wadsworth (2018). Modeling spatial processes with unknown extremal dependence class. *Journal of the American Statistical Association*. To appear.
- Ibragimov, I. A. and K. E. Chernin (1959). On the unimodality of stable laws. *Teor. Veroyatnost. i Primenen.* 4, 453–456.
- Jolliffe, I. T. (2002). *Principal component analysis* (Second ed.). Springer Series in Statistics. Springer-Verlag, New York.
- Kabluchko, Z., M. Schlather, and L. de Haan (2009). Stationary max-stable fields associated to negative definite functions. *Ann. Probab.* 37(5), 2042–2065.
- Kanter, M. (1975). Stable densities under change of scale and total variation inequalities. *Ann. Probability* 3(4), 697–707.
- Kuss, M. and C. E. Rasmussen (2005). Assessing approximate inference for binary Gaussian process classification. *J. Mach. Learn. Res.* 6, 1679–1704.

- Morris, S. A. (2016). *Spatial Methods for Modeling Extreme and Rare Events*. Thesis (Ph.D.) North Carolina State University.
- Oesting, M. (2018). Equivalent representations of max-stable processes via ℓ^p -norms. *J. Appl. Probab.* 55(1), 54–68.
- Opitz, T., R. Huser, H. Bakka, and H. Rue (2018). INLA goes extreme: Bayesian tail regression for the estimation of high spatio-temporal quantiles. *Extremes*. To appear.
- Perica, S., D. Martin, S. Pavlovic, I. Roy, M. S. Laurent, C. Trypaluk, D. Unruh, M. Yekta, and G. Bonnin (2013). NOAA atlas 14 volume 9 version 2, precipitation-frequency atlas of the united states, southeastern states. *NOAA, National Weather Service* 9, 18.
- Reich, B. J. and B. A. Shaby (2012). A hierarchical max-stable spatial model for extreme precipitation. *Ann. Appl. Stat.* 6(4), 1430–1451.
- Resnick, S. I. (1987). *Extreme values, regular variation, and point processes*, Volume 4 of *Applied Probability. A Series of the Applied Probability Trust*. Springer-Verlag, New York.
- Schlather, M. and J. A. Tawn (2003). A dependence measure for multivariate and spatial extreme values: properties and inference. *Biometrika* 90(1), 139–156.
- Shaby, B. and M. Wells (2010). Exploring an adaptive Metropolis algorithm. Technical Report 1011-14, Duke University Department of Stastical Science.
- Stephenson, A. G. (2009). High-dimensional parametric modelling of multivariate extreme events. *Aust. N. Z. J. Stat.* 51(1), 77–88.
- Suro, T. P., G. D. Firda, and C. O. Szabo (2009). Flood of june 26-29, 2006, mohawk, delaware, and susquehanna river basins, new york. *US Geological Survey Open-File Report 1063*, 354.
- Thibaud, E. and T. Opitz (2015). Efficient inference and simulation for elliptical Pareto processes. *Biometrika* 102(4), 855–870.